



The haze and methane distributions on Uranus from HST-STIS spectroscopy

Erich Karkoschka*, Martin Tomasko

Lunar and Planetary Laboratory, University of Arizona, Tucson, AZ 85721-0092, United States

ARTICLE INFO

Article history:

Received 19 July 2008

Revised 9 February 2009

Accepted 13 February 2009

Available online 26 February 2009

Keywords:

Uranus

Spectroscopy

ABSTRACT

We analyzed a unique, three-dimensional data set of Uranus acquired with the STIS Hubble spectrograph on August 19, 2002. The data covered a full afternoon hemisphere at 0.1 arc-sec spatial resolution between 300 and 1000 nm wavelength at 1 nm resolution. Navigation was accurate to 0.002 arc-sec and 0.02 nm. We tested our calibration with WFPC2 images of Uranus and found good agreement. We constrained the vertical aerosol structure with radiative transfer calculations. The standard types of models for Uranus with condensation cloud layers did not fit our data as well as models with an extended haze layer. The dark albedo of Uranus at near-infrared methane windows could be explained by methane absorption alone using conservatively scattering aerosols. Ultraviolet absorption from small aerosols in the stratosphere was strongest at high southern latitudes. The uppermost troposphere was almost clear, but showed a remarkable narrow spike of opacity centered on the equator to 0.2° accuracy. This feature may have been related to influx from ring material. At lower altitudes, the feature was centered at $1\text{--}2^\circ$ latitude, suggesting an equatorial circulation toward the north. Below the 1.2 bar level, the aerosol opacity increased some 100 fold. A comparison of methane and hydrogen absorptions contradicted the standard interpretation of methane band images, which assumes that the methane mixing ratio is independent of latitude and attributes reflectivity variations to variations in the aerosol opacity. The opposite was true for the main contrast between brighter high latitudes and darker low latitudes, probing the 1–3 bar region. The methane mixing ratio varied between 0.014 and 0.032 from high to low southern latitudes, while the aerosol opacity varied only moderately with latitude, except for an enhancement at -45° latitude and a decrease north of the equator. The latitudinal variation of methane had a similar shape as that of ammonia probed by microwave observations at deeper levels. The variability of methane challenges our understanding of Uranus and requires reconsideration of previous investigations based on a faulty assumption. Below the 2 bar level, the haze was thinning somewhat. Our global radiative transfer models with 1° latitude sampling fit the observed reflectivities to 2% rms. The observed spectra of two discrete clouds could be modeled by using the background model of the appropriate latitude and adding small amounts of additional opacity at levels near 1.2 bar (southern cloud) and levels as high as 0.1 bar (northern cloud). These clouds may have been methane condensation clouds of low optical depth (~ 0.2).

© 2009 Elsevier Inc. All rights reserved.

1. Introduction

Uranus is the planet with the clearest upper troposphere. All other planets with significant atmospheres, as well as Titan, have hazes or clouds with significant optical depth in the uppermost scale height of the troposphere, in the case of Neptune at least at some locations. On Uranus, the aerosol optical depth is only on the order of 0.01 in this altitude range. In the next scale height further down, the aerosol optical depth remains below 0.1. The lack of significant aerosols makes Rayleigh scattering the dominant opacity below about 600 nm wavelength, which makes the planet almost perfectly featureless at these wavelengths. Voyager 2 images in this

wavelength range during the 1986 fly-by caused Uranus to be considered the blandest planet.

In the 1990s, the Hubble Space Telescope (HST) at longer wavelengths with thus reduced Rayleigh opacity revealed major latitudinal and discrete structures. With the more recent addition of adaptive optics imaging at Keck, Uranus became known as a very dynamic planet (Rages et al., 2004; De Pater et al., 2002; Hammel et al., 2005; Sromovsky and Fry, 2005, 2007, 2008).

The weakness of aerosol opacity on Uranus complicates deriving its vertical distribution. On other giant planets and on Titan, where aerosol opacity typically dominates Rayleigh scattering opacity, methane band spectroscopy has yielded pressure levels of haze and clouds with uncertainties similar to that of methane absorption coefficients. For Uranus, Rayleigh opacities are large and magnify uncertainties of coefficients. Furthermore, constraining the

* Corresponding author. Fax: +1 520 621 4933.

E-mail address: erich@lpl.arizona.edu (E. Karkoschka).

vertical structure requires observations of different absorptions, which increases uncertainties even more.

In order to make some progress in radiative transfer modeling of Uranus, other knowledge has been incorporated into the models. Rages *et al.* (1991) used Voyager 2 data and incorporated a cloud physics calculation about haze in the upper atmosphere. Methane was expected to form a cloud near 1.4 bars, and the Voyager occultation data (Lindal *et al.*, 1987) showed some indication of a methane cloud. This approach produced models with a high haze layer and two cloud layers below at the methane condensation level and near 3 bars. This model was modified by the inclusion of high resolution spectroscopy (Baines *et al.*, 1995), Keck imaging (Sromovsky and Fry, 2007), and near-infrared spectroscopy (Irwin *et al.*, 2007; Sromovsky and Fry, 2008).

As the data improved, the standard model for Uranus had problems. The upper cloud was shown to be lower than the methane condensation layer (Sromovsky and Fry, 2007), and no other species were expected to condense at that layer. Furthermore, radio data by Hofstadter and Butler (2003) suggested a global circulation with rising air and condensation clouds at low latitudes and descending air and clearer conditions at high latitudes. This circulation is consistent with the observed distribution of discrete cloud features occurring mostly within 45° of the equator. However, all previous models had the cloud opacity just opposite, which seemed unavoidable because methane band images showed a bright polar region versus a dark low-latitude region.

Uranus poses other challenges. On Jupiter and Saturn, methane is expected to be uniformly mixed throughout the troposphere at all latitudes. Thus, the distribution of aerosol opacity can be directly inferred from methane band imaging. On Uranus, the methane mixing ratio in the upper troposphere varies vertically by three orders of magnitude, similar to water on Earth. The terrestrial water mixing ratio also varies by orders of magnitude with latitude and time, which may be true for methane on Uranus as well. However, because of the lack of data, methane has been assumed to be constant with latitude and time. If this assumption were wrong, aerosol opacities could be off by large factors. This uncertainty can be avoided by observing hydrogen absorptions, which requires spectroscopy since few available filters probe hydrogen absorptions.

Uranus poses more challenges. In the 600–1000 nm wavelength region, albedos of Jupiter and Saturn are primarily dependent on methane absorption coefficients, while albedos of Titan and Uranus display another, strong spectral dependence, which is not well understood. For Titan, this led to models of a mostly clear troposphere which was corrected by data from the Huygens probe. For Uranus, such pitfalls could be avoided by using spectroscopy probing sufficiently many wavelengths in order to decouple both spectral dependencies.

The misconception about Titan's troposphere was also caused by insufficient knowledge of methane absorption coefficients. Most investigations of the opacity structure of Uranus relied on methane absorption coefficients, such as those by Irwin *et al.* (2006), with large extrapolations from conditions in the laboratory to those on Uranus. The three parameters of pressure, temperature, and methane pathlength required smaller, similar, and larger extrapolations for Uranus than for Titan, respectively. Unfortunately, the Huygens measurements proved the extrapolation methods to be unreliable for Titan (Tomasko *et al.*, 2008), especially at wavelengths above $1\ \mu\text{m}$ suitable for adaptive optics systems. One can interpret methane data without knowledge of these coefficients, but such methods require spectroscopy.

We designed observations to address these challenges of modeling Uranus. We took the observations into new terrain. The Space Telescope Imaging Spectrograph (STIS) aboard the Hubble Space Telescope (HST) offered the ability to combine the power of spec-

Table 1
Observations.

Date	2002 August 19, 1:43–10:57 UT
Radius of Uranus	1.86 arc-sec
Line of sight	20.5° below equator of Uranus
Phase angle	0.04°
Program ID	GO 9035
Instrument	HST-STIS
Gratings	G430L (290–570 nm), G750L (530–1020 nm)
Dispersion	$0.27\ \text{nm}(\text{pixel})^{-1}$ (G430L) and $0.49\ \text{nm}(\text{pixel})^{-1}$ (G750L)
Spectral resolution	1 nm
Slit width	0.1 arc-sec
Pixel size	0.05 arc-sec (north–south on Uranus)
East–west sampling for G430L	13 exposures spaced 0.15 arc-sec
East–west sampling for G750L	40 exposures spaced 0.05 arc-sec
Exposure time	87 s per exposure on Uranus
Exposure level	600 electrons per data point (median)

troscopy with the high spatial resolution of HST. This work describes how a data cube acquired in 2002 changed our view about the methane and aerosol opacity structure of Uranus.

Section 2 describes the observations and data analysis. Section 3 reports observed latitudinal variations. Section 4 gives our radiative transfer modeling technique. Section 5 discusses modeling results about aerosol properties, and Section 6 about the aerosol vertical distribution. Section 7 focuses on two discrete clouds. Section 8 summarizes our work.

2. Data reduction

2.1. Observations

On August 19, 2002, the Space Telescope Imaging Spectrograph (STIS) took 63 images for our program GO 9035. The three-orbit program was executed during seven successive, shortened HST orbits. The first exposure was an acquisition image with a pass-band of 530–1000 nm wavelength (filter F28X52LP). Following were 13 exposures with the grating G430L covering the wavelengths 290–570 nm at $0.27\ \text{nm}(\text{pixel})^{-1}$. The slit was 0.1 arc-sec wide and parallel to the central meridian of Uranus, stepping from the evening limb to the central meridian in 0.15 arc-sec intervals. Along the slit, 140 samples were taken, of which Uranus took up to 73 pixels at $0.05\ \text{arc-sec}(\text{pixel})^{-1}$. Following was a lamp exposure for wavelength calibration. The remaining exposures used the grating G750L covering the wavelengths 530–1020 nm at $0.49\ \text{nm}(\text{pixel})^{-1}$. These observations were similar to the G430L observations, except that the slit was positioned at 40 locations from the evening limb to the central meridian in 0.05 arc-sec intervals. A lamp exposure and flatfield each were taken during four times of this sequence. The observational parameters are summarized in Table 1.

2.2. Flatfielding

The standard pipeline processing by the Space Telescope Science Institute (STScI) provides bias subtraction and standard flatfielding. We used an automatic routine adjusted to our data set to identify bad pixels, almost all of them due to hits by cosmic rays. We restored 36,285 pixel values (0.4% of all pixel values) by interpolation from good pixels.

The standard flatfielding does not take into account that the slit width varies on small scales by typically 1–2% with one spot of a 20% variation. We averaged flatfields spectrally to obtain the slit width function. The slit features shifted by 1.4 and 0.4 pixels when gratings were changed or calibration exposures were taken. The slit width function was accordingly shifted before applied to

all data. All interpolations used cubic interpolation based on the eight nearest points.

Above 700 nm wavelength, the CCD displays fringing of up to 30% amplitude in intensity, which is poorly divided out in the standard flatfielding due to wavelength shifts between different observations. The pattern of fringes was taken from the average of the four flatfields after the general spectral dependence on large scales (>50 pixels) was divided out. To reduce noise further, this image was smoothed using pixels within a radius of 3 pixels. The fringe amplitude was increased by 10% since it had been decreased by a similar amount due to scattered light. Fringes in Uranus frames completely disappeared after the correction was applied. This correction was dependent on measured wavelength shifts as explained later.

2.3. Charge transfer efficiency

The STIS CCD is known to have a charge transfer efficiency significantly less than unity, getting worse from year to year but improving with increasing exposure levels (Goudfrooij et al., 2006). It creates an asymmetry in the sky intensity with rows below Uranus (smaller row numbers) appearing brighter than above. We measured the asymmetry and found the deviation of charge transfer efficiency from unity to be roughly proportional to the maximum signal in the column to the power -0.4 , similar to exponents between -0.3 and -0.4 measured by Goudfrooij and Kimble (2002). The shape of the asymmetry indicated an exponential decay with an $1/e$ length of 20 pixels. The total signal lost was estimated at 1% for the highest signals of $10,000 \text{ electrons}(\text{pixel})^{-1}$ (acquisition image) to 10% for low signals near $30 \text{ electrons}(\text{pixel})^{-1}$ (deep methane bands). For each column, deconvolution with the appropriate exponential function brought the lost signal back to its origin, and the sky intensities became close to symmetric.

2.4. Light scattered in the CCD

The STIS CCD is a backside illuminated chip, which creates wide halos, especially longward of 750 nm wavelength. Quijano et al. (2007) suggested the scatter to occur within the CCD mounting substrate. They give the fractional energy in the halo of $\sim 20\%$ (805 nm) and $\sim 30\%$ (905 nm), but no spatial distribution, which is essential for Uranus data. The scattering is obvious by comparing the signal in the sky between exposures on Uranus and those off the limb. We performed trial deconvolutions with the Wiener method varying the size and shape of the point spread function (PSF) for the halo, until the sky signal decreased to the much smaller diffraction level. This occurred when the PSF was the Fourier transform of

$$1 - 1/(50 + 1/f) - [(\lambda - 570)/60]^2/(200 + 1/f), \quad (1)$$

where f is the spatial frequency, λ is the wavelength in nm, and the $(\lambda - 570)$ term is set to zero for wavelengths below 570 nm. Equation (1) indicates a general scattering of 15% fractional energy with a length scale of 50 pixels and a spectrally dependent scattering with a length scale of 200 pixels, increasing from zero at 570 nm to 20% at 1000 nm. We performed deconvolutions for 16 values of λ in Eq. (1) and used linear interpolation in between.

2.5. Spectral calibration

We adopted the distortion of STIS images including the spectral nonlinearity by McGrath et al. (1998), except that we used our own measurements of calibration exposures for the first-order terms, which both indicated a rotation of 0.02° less than McGrath's. We rectified all images.

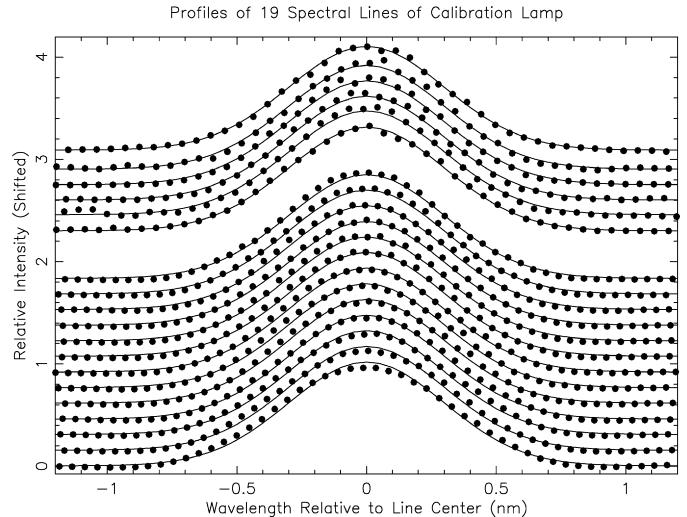


Fig. 1. Profiles of 19 spectral lines of the calibration lamp, six lines from the G430L spectra (top) and 13 lines from the G750L spectra (bottom). The curves are Gaussian with 0.7 nm FWHM, which provided a good fit throughout the probed spectrum.

In the raw lamp images, the 0.36° tilt between the spectral lines and the CCD columns caused a shift by one pixel every 160 rows. Combining data of all rows provided the spectral line profile at 160 samples per pixel. It was almost independent of wavelength. Most of the width of the profile was due to the slit width of two pixels. On a pixel scale, the resolution was 10% better for the G750L than G430L spectra. On a wavelength scale, it was opposite by a factor of 1.6. In order to create a data set of constant resolution, we smoothed the G430L spectra with a kernel of 0.3, 0.4, 0.3 and slightly sharpened the G750L spectra with a kernel of $-0.1, 1.2, -0.1$. The resulting line profiles (Fig. 1) were all close to Gaussian of 0.70 nm full width at half maximum (FWHM). This profile causes similar smoothing as a 1 nm wide rectangular profile, corresponding to 1 nm spectral resolution if the sampling interval remains below 0.5 nm. We reduced the total wavelength range slightly to 300–1000 nm, taking 1750 samples every 0.4 nm, since data outside this range were too noisy and only useful for checks of scattered light. Near the spectral endpoints, noisy data became useful through sufficient spectral and spatial averaging.

The lamp exposures provided the spectral resolution for a fully illuminated slit. We estimated the illumination of the slit for each location on Uranus and inferred the resulting spectral sharpening. To counteract this effect, we smoothed the spectra accordingly. Careful accounting of the spectral resolution is critical for Raman scattering analysis, where a slight decrease of spectral resolution fills in solar Fraunhofer lines and thus mimics Raman scattering.

We accounted for the rotation of Uranus and the motion of HST around the Earth, causing a shift of solar lines and a stretch of the spectral scale by typically 0.05 pixels. The shift between methane bands of Uranus and reflected solar lines was only about 0.01 pixels and thus ignored.

Because of flexure inside the STIS spectrograph over the course of our observations, we measured spectral shifts for each exposure on Uranus based on positions of the solar H and K Fraunhofer lines for the G430L spectra, and the H_α line for the G750L spectra. Our measurement routine used the whole line profiles. We accounted for the expected shift due to non-uniform illumination of the slit, which was typically less than 0.2 pixels. Within each orbit, measured positions scattered by 0.02–0.03 pixels root-mean-square (rms), consistent with data noise and a stable instrument. Real spectral shifts of about 0.1 pixels occurred in between orbits (cf. Fig. 2).

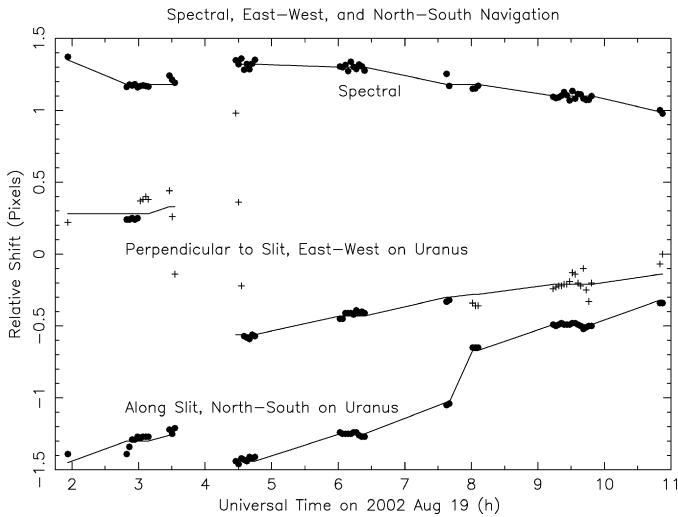


Fig. 2. Three dimensional navigation of the whole data set. Reliable measurements are plotted as circles, less reliable ones as crosses. The adopted functions are shown as lines. In all three dimensions, the filled circles scatter by 0.02 pixels rms around the lines, the precision of navigation.

Our adopted spectral flexure of the spectrograph (top line in Fig. 2) differs by 0.023 pixels rms from the data points, corresponding to 0.006 nm (G430L) and 0.011 nm (G750L). We estimated the spectral calibration to be accurate to 0.02 nm. Consistency tests of our wavelength calibration were satisfying, e.g. checking ratios between G430L and G750L spectra. Since HST is in space, we used vacuum wavelengths, which are up to 0.3 nm longer than air wavelengths.

2.6. Spatial calibration

In this work, we use the cardinal direction on Uranus with the visible pole in 2002 defined as the south pole. We determined the north-south location on Uranus along the slit with two methods. Using the spectral response of the acquisition filter, we spectrally integrated each of the G750L images into a spatial intensity profile. By comparing this profile with north-south cuts through the acquisition image, we navigated each image to about 0.04 pixel accuracy. We then applied this method to the G430L images by comparing spatial profiles in the overlapping spectral region, which was accurate to 0.08 pixels considering the need of two steps. The other method used wavelengths where Uranus displays close to perfect north-south symmetry and a relatively sharp limb. This method was accurate to about 0.04 pixels.

Both methods agreed to 0.05 pixels for each wavelength range. We plot the mean of both methods at the bottom of Fig. 2. These data points scatter by 0.02 pixels rms within each orbit, but shift by ~ 0.1 pixel in between. It indicates that during each orbit, HST tracked Uranus to about 0.001 arc-sec in the direction along the slit. We estimated the adopted north-south navigation (bottom line in Fig. 2) to be accurate to 0.04 pixels, corresponding to 0.002 arc-sec. We subsampled the navigated data at 0.015 equatorial radii of Uranus, corresponding to 0.028 arc-sec (original pixel size 0.05 arc-sec). For a few observations near the limb, spatial profiles were too smooth to navigate. Their adopted navigation came from nearby exposures.

A shift of 0.4 pixels occurred just before 8 o'clock (cf. Fig. 2) during calibration exposures, requiring a physical motion in the spectrograph. At the same time, the recorded flatfield streaks due to slit-width variations shifted also by 0.4 pixels, indicating a cause inside the spectrograph.

We determined the distance between the slit and the central meridian of Uranus for each exposure. We used the acquisition im-

age for comparison of spatial profiles, similar to the first method for the north-south navigation. For the images between the limb and the halfway point to the central meridian, the measurements scattered by 0.025 pixels within each orbit (dots near center of Fig. 2). Our adopted east-west navigation (center line in Fig. 2) is estimated to be as accurate as the north-south navigation.

Within each orbit, the east-west offsets between successive images were as large as the commanded offsets within our uncertainties. In between orbits, measured offsets were 0.1–0.2 pixels smaller than commanded, indicating a constant drift between orbits, similar to the north-south drift (Fig. 2). We used this drift rate to extrapolate the east-west navigation to images which could not be directly navigated well (crosses in Fig. 2), and where east-west navigation is less critical since reflectivities change only slowly with east-west location (aside from discrete features). This method found the first G430L image and the first two G750L images positioned just off the limb. The last slit location of both sequences occurred within 0.02 arc-sec of the central meridian. Thus, our data covered the complete afternoon hemisphere of Uranus.

All our spatial sampling occurred at 0.05 arc-sec, except for the 0.15 arc-sec east-west sampling of the G430L data which is worse than the resolution of about 0.1 arc-sec. Since Uranus was almost featureless at these wavelengths, we were able to use two interpolation techniques adding the missing data. First, we used quadratic interpolation roughly in east-west direction, but tilted somewhat near the limb toward a direction parallel to the limb. Second, we used linear interpolation parallel to the elliptical limb of Uranus.

We tested both methods with the acquisition image by reconstruction using only data for one out of every three columns. This test was sensitive since the acquisition image displayed stronger features than the G430L data. Our test suggested satisfying results for our adopted method, which used the first method for the 10 intervals closest to the central meridian, the mean of both methods for the following interval, and the second method further outside. Because interpolation cannot be perfect, we did not use data close to the limb on small latitudinal scales for modeling wavelengths below 530 nm.

The 100 wavelength samples between 530 and 570 nm observed with both gratings allowed sensitive cross checks of our spatial calibrations. Subtracting image pairs for the same wavelength revealed small differences: the G750L images indicated a slightly sharper evening limb than the G430L images, which could be explained by east-west navigational offsets of about 0.001 arc-sec. Furthermore, the sky intensity was correlated with the time difference between the observations and the passage of HST through the South Atlantic Anomaly. The size of this effect was on the order of 0.1% of the intensity on the disk.

The rings of Uranus appeared as a dark streak tilted at a different angle than northern latitude bands, in particular at continuum wavelengths. We estimated the two-way ring transmission as function of radius from Uranus based on French et al. (1991) and convolved this function by our PSF. We divided our data numbers by this function. The maximum correction was 1.6%. No hint of the rings remained at the 0.2% level, the level of some artifacts. Light from the rings was barely detectable in the sky and not detectable on the disk. It was negligible.

2.7. Telescope diffraction

The PSF of HST has significant diffraction wings. About 75% of the energy of the PSF is within 0.2 arc-sec radius, another 20% is out to 2 arc-sec radius, and the remaining 5% is further out. Since these fractions vary with wavelength, interpretation of raw images is cumbersome. The PSF is very stable, unlike PSFs of adaptive optics systems. This allows accurate deconvolution to a spectrally constant PSF. For deconvolution to work properly at the edges of

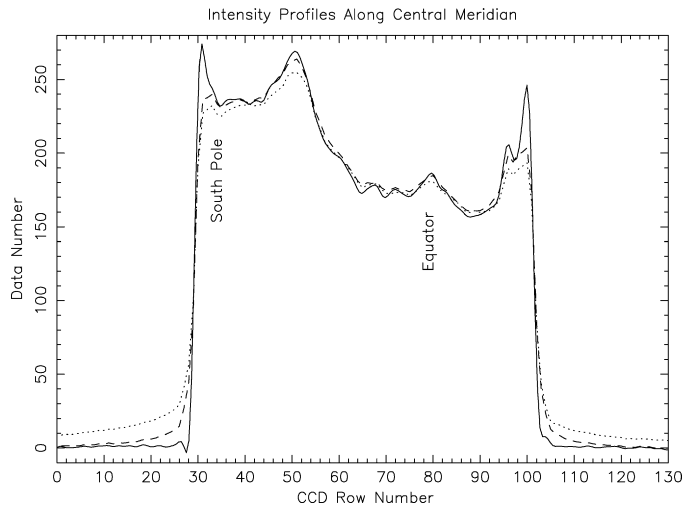


Fig. 3. Intensity profiles along the central meridian near 800 nm wavelength. The dotted curve shows the raw data. Deconvolution accounting for the CCD charge transfer efficiency and light scattering yields the dashed curve. Deconvolution of the HST diffraction yields the solid curve.

images, we expanded the hemispheric images to full-disk images using east–west symmetry.

We created synthetic, monochromatic PSFs with the TinyTIM software provided by STScI (Krist, 2004) at 18 wavelengths, spaced by 40 nm. Linear interpolation provided a PSF for each of our 1750 wavelengths. We then smeared each PSF in the east–west direction by the slit width of 0.1 arc-sec. Using the Wiener method, we deconvolved each image with the corresponding PSF and convolved the result with a constant PSF which is similar to a Gaussian with 0.08 arc-sec FWHM. This PSF has more than 99% of the signal within a radius of 0.1 arc-sec, far better than the $\sim 50\%$ value for the original PSFs. It is a radial symmetric PSF, unlike the original elongated PSFs. Noise and image sharpness were only moderately affected since the FWHM of the final PSF (0.08 arc-sec) is similar to the FWHM of the original PSFs, ranging from 0.10×0.06 arc-sec (east–west \times north–south) at 300 nm to 0.14×0.10 arc-sec at 1000 nm wavelength.

Data numbers of the sky became smaller than 0.5% of the data numbers on Uranus, a 40-fold improvement over the raw images due to three deconvolutions: charge transfer efficiency, scattered light in the CCD, and telescope PSF. Aside from minor “ringing” within a few pixels of the limb, which is typical for deconvolutions, no significant structure was apparent in the sky (light from the rings was negligible and no bright satellite was in the slit). An example of deconvolutions is displayed in Fig. 3. Sky levels were strongly decreased and significant limb brightening becomes evident, which was not the case in the raw image.

2.8. Center-to-limb fitting

For comparison with radiative transfer models, useful spatial coordinates on Uranus are latitude and center-to-limb position which is described in this work by the cosine of the emission angle μ . The reflectivity as function of μ can be approximated by a Minnaert law ($I/F = C\mu^{2k-1}$ for zero phase angle), which has two free parameters. The top of Fig. 4 shows that Minnaert fits (dashed and dashed-dotted) do not work well across a large range of μ . Thus, we tested four functions with three free parameters for our data set. Our adopted center-to-limb functions are linear combinations of three Minnaert functions with a limb darkening exponent k of 0, 0.5, and 1. Observed values of k for all combinations of latitudes and wavelengths were between 0 and 1.

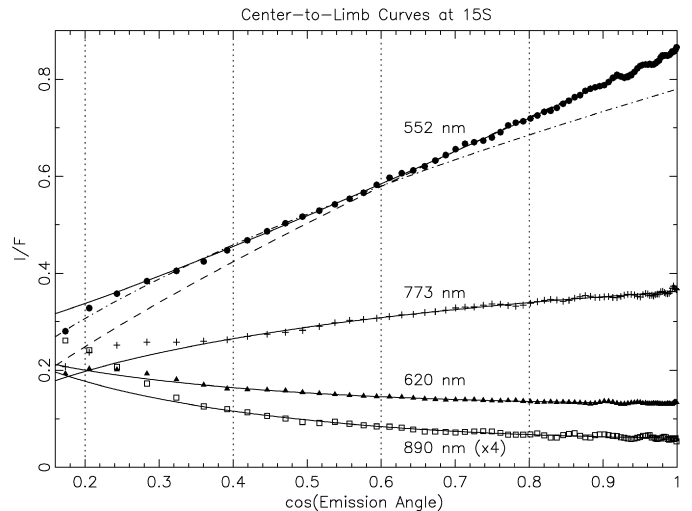


Fig. 4. Limb darkening data at four wavelengths for the latitude region 15S (symbols). The solid curves show fits with the three-parameter function, which work well in the 0.3–1 region of μ . For the 552 nm data, two fits with Minnaert functions are shown too (dotted and dashed-dotted), which can either fit smaller or larger emission angles, but not both at the same time.

We created synthetic images for $k = 0.5$ and 1 and convolved them with the PSF of the processed images. The convolved $k = 0.5$ image gave the reflectivity correction near the limb due to the finite size of the PSF, which we corrected for. The ratio between both convolved images gave the effective μ for each pixel. A similar method produced effective latitudes by using latitudes as data numbers for the synthetic $k = 1$ image. The effective quantity q_{eff} (latitude or μ) at a specific pixel is

$$q_{\text{eff}} = \iint q(x, y) \text{PSF}(x, y) dx dy / \iint \text{PSF}(x, y) dx dy, \quad (2)$$

where $\text{PSF}(x, y)$ is the PSF centered on the pixel and the integrations go over the disk of Uranus. For example, the pixel centered on the south pole probes latitudes between -85 and -90° and has an effective latitude of -87° .

We calculated the three-parameter center-to-limb curves for each wavelength and latitude using the least square method. Pixels near the limb of Uranus got a reduced weighting factor. Our linear functional form allowed analytical solutions, while fitting functions such as Minnaert laws requires slower iterations. Four selected wavelengths at latitude -15° are featured in Fig. 4. The fits are very close to the data points for $\mu > 0.4$, fairly close for μ near 0.3, but deviate significantly for μ near 0.2. Note that $\mu = 0.4, 0.3$, and 0.2 corresponds to 0.15, 0.07, and 0.03 arc-sec from the limb of Uranus, respectively. Our fits are accurate to 0.1 arc-sec from the limb.

This work uses the reflectivities of the fitted curves at $\mu = 0.4, 0.6$, and 0.8 (vertical dotted lines in Fig. 4) rather than single data points, which diminishes noise or small-scale structure seen in Fig. 4. This choice stays away from the uncertainties very close to the limb, and it does not use values $\mu > 0.8$ which are only observable for a small range of latitudes near the center of the disk. Reflectivity ratios between $\mu = 0.8$ and 0.4 are a measure of the limb darkening, called here the *Limb Darkening Ratio*. It is unity for a disk of constant brightness, it takes the value of two for Lambert limb darkening, and it is less than unity for limb brightening.

To extend our data sampling to the limb of Uranus, we averaged all data within 0.1 arc-sec of the limb. This average represents the reflectivity near $\mu = 0.2$, somewhat dependent on the slope of the center-to-limb curve. Based on measured slopes and simulations, we approximately corrected for this effect. We used reflectivities at $\mu = 0.2$ only for qualitative results.

In summary, for each wavelength and latitude, we obtained fitted reflectivities at $\mu = 0.2, 0.4, 0.6$, and 0.8 . We call these reflectivities I_2/F , I_4/F , I_6/F , and I_8/F , respectively, and the ratio I_8/I_4 is our measure of limb darkening. While most observed latitudes included data at $\mu = 0.2$ and 0.4 , only latitudes $-74^\circ \dots +33^\circ$ included data at $\mu = 0.6$, further narrowing to $-58^\circ \dots +17^\circ$ for $\mu = 0.8$. We restrict most of our results to these limited latitude ranges, but occasionally show small extrapolations where we estimated them to be fairly reliable.

Out of the ~ 7000 pixels on the disk of Uranus in calibrated images, 111 pixels had elevated data numbers near four discrete features and were thus excluded from all fits described above.

2.9. Albedo calibration

The STIS Data Handbook (Dressel et al., 2007) provides the conversion between data numbers and absolute flux as a function of wavelength. Using the solar flux spectrum by Colina et al. (1996), the flux was converted to reflectivities I/F . Spatial summation yielded the geometric albedo of Uranus as function of wavelength. A comparison between G430L and G750L data in the overlapping 530–570 nm region indicated a calibration offset of less than 2% and a scatter of 0.9% rms, excluding data near the edge of the spectral range. Above 540 nm wavelength, we adopted the G750L images because their finer east–west sampling, considering the presence of latitudinal features in the 543 nm methane band. Between 530 and 540 nm, we created a smooth transition by weighting the G750L images linearly increasing from 0 to 100%.

HST images have provided absolute intensity calibration with an exceptional accuracy and stability for point sources as well as extended sources. For the STIS spectrograph, the albedo calibration only applies to the standard reduction technique appropriate for sources smaller than the slit width. Since Uranus was 40 times larger than the slit width, the three sources causing spatial smoothing (charge transfer efficiency, CCD scattering, and telescope diffraction) may offset the absolute intensity calibration. Since these three effects are smooth functions of wavelength, the calibration offset is also expected to be spectrally smooth. We used images taken with the Wide Field and Planetary Camera 2 (WFPC2) to define the offset as function of wavelength.

The closest HST imaging of Uranus to our 2002 data with the required spectral coverage occurred on August 29, 2003 with nine WFPC2 filters (GO 9725, PI Karkoschka). We adopted the calibration technique for images taken in 1997 with the same filters (Karkoschka, 2001). We linearly interpolated both WFPC2 data sets to the date of the STIS data set since the temporal change of Uranus was roughly linear during this period (Lockwood and Jerzykiewicz, 2005).

In order to compare WFPC2 and STIS data, we convolved our STIS data with the spectral throughput curves of each WFPC2 filter, including the solar flux spectrum. Initial STIS albedos were lower than WFPC2 albedos, by 15% in the ultraviolet, increasing to more than 30% in the near-infrared (triangles in Fig. 5), with a smooth spectral variation as expected. Fig. 5 displays our adopted correction function, a polynomial of order two, which we applied to all reflectivities. The nine data points scatter by 1.8% rms around the adopted curve. Excluding the unreliable filter FQCH4N-D (cf. Karkoschka and Koekemoer, 2002), the scatter decreases to 1.3% rms. Thus, our corrected absolute calibration was closely tied to the WFPC2 calibration (Karkoschka, 2001), accurate to about 5%. A rough calibration of the same data set by Fry and Sromovsky (2007) found a similar calibration level with a somewhat larger spectral dependence.

Fig. 5 ratios spectra from STIS and ESO (European Southern Observatory) taken in 1995 (Karkoschka, 1998a). The comparison is satisfactory, considering the temporal variation during the seven

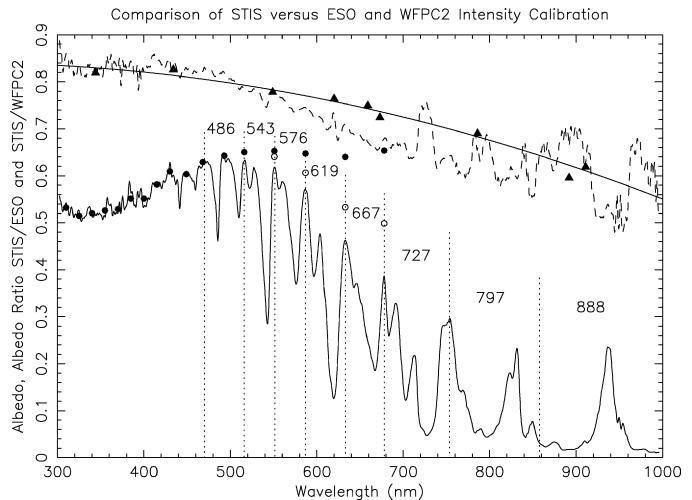


Fig. 5. Uranus geometric albedos from the initial STIS calibration divided by albedos from WFPC2 (triangles) or by the Uranus spectrum observed at ESO (dashed curve). The smooth solid curve shows the adopted correction for STIS albedos. The bottom curve displays the geometric albedo spectrum of Uranus. Continuum wavelengths are marked for nominal methane absorption coefficients (open circles) and slightly adjusted coefficients (solid circles). The vertical dotted lines mark the boundaries between eight labeled methane bands. The triangles correspond to the nine WFPC2 filter names listed in Fig. 6.

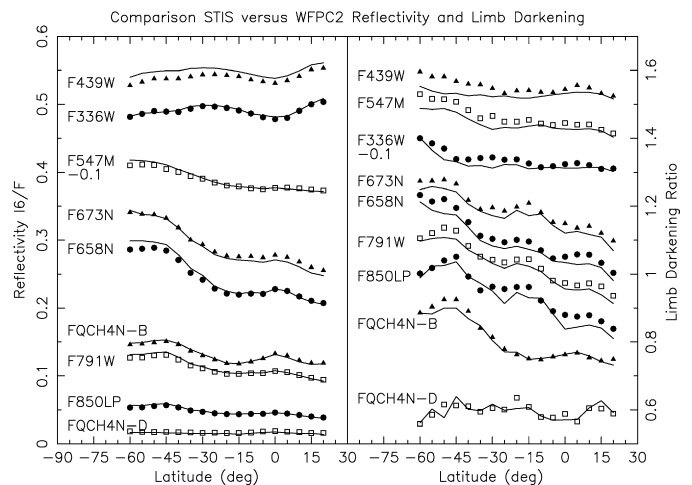


Fig. 6. Comparison of latitudinal profiles from STIS (curves) and from WFPC2 (symbols). The left panel displays reflectivities, the right panel the Limb Darkening Ratio. Typical deviations between STIS and WFPC2 data are 1% for the reflectivity and 0.02 for the Limb Darkening Ratio.

years between both data sets expected in particular at longer wavelengths.

The WFPC2 images also allow a sensitive test of the complicated navigation of STIS data and its influence on center-to-limb fits. We applied our fitting routine to the nine WFPC2 images. The resulting reflectivity I_6/F and Limb Darkening Ratio (I_8/I_4) as function of latitude are compared in Fig. 6 with STIS data. Reflectivities typically agree to 1%. Limb Darkening Ratios are typically about 0.02 lower for STIS than for WFPC2, and their latitudinal variations are consistent to about 0.01. This is an excellent agreement since Limb Darkening Ratios accurate to 0.02 allow powerful constraints for radiative transfer models. The small differences may come from imperfect synthetic PSFs for HST and changes on Uranus from 2002 to 2003. A similar comparison with 13 ACS images taken one day after the WFPC2 images was also satisfactory.

Table 2

Sampling of reduced reflectivities.

Latitudes (planetographic): 140 samples every 1° from -84° to $+55^\circ$; six representative regions: “60S” $-67^\circ \dots -53^\circ$, “46S” $-51^\circ \dots -41^\circ$, “33S” $-39^\circ \dots -27^\circ$, “15S” $-25^\circ \dots -5^\circ$, “1N” $-4^\circ \dots +6^\circ$, “25N” $+18^\circ \dots +32^\circ$.

Center-to-limb data: $\mu = \cos(\text{emission angle}) = 0.2, 0.4, 0.6, 0.8$.

Continuum wavelengths: 15 bands centered at 310, 325, 340, 355, 370, 385, 400, 415, 430, 449, 468, 493, 516, 551, 587 nm.

Methane absorption wavelengths: 55 spectral bands for eight methane bands (486, 543, 576, 619, 667, 727, 797, 888 nm) and 16 methane absorption coefficients every factor of two from 0.001 to 32 $\text{km}\cdot\text{am}^{-1}$, cf. Fig. 8 for combinations of both parameters.

Hydrogen absorption wavelengths: 10 bands between 819 and 835 nm, each 1.6 nm wide.

In summary, the absolute reflectivity calibration of our data set is accurate to 5%. Relative reflectivities between different latitudes or nearby wavelengths are accurate to about 1%. Limb Darkening Ratios are accurate to 0.02.

2.10. Raman scattering

Raman scattering causes photons to occasionally lose part of their energy during a scattering process; they are reflected at a longer wavelength. This causes a net loss of reflected photons at most ultraviolet wavelengths and a net gain at deep solar Fraunhofer lines. Ideally, Raman scattering is calculated in radiative transfer models at hundreds of wavelengths, keeping track of photons jumping to longer wavelengths. This enormous complication with some 100-fold increased running times is rarely performed. Sromovsky (2005) investigated previous approximation methods. We adopted the method by Karkoschka (1998a), where the net gain and loss of photons is estimated at every wavelength, and then the observations are corrected for this effect. Sromovsky (2005) found this method quite accurate at ultraviolet wavelengths, and somewhat less accurate at longer wavelengths, in particular at the weakest methane bands.

Using Sromovsky’s results, we improved our previous method longward of 500 nm wavelength. We changed the exponent for the spectral dependence from -0.5 to -2 until 550 nm, then to -3 until 600 nm, and to -4 beyond. It is expected to approach the Rayleigh exponent of -4 at long wavelengths. Above 500 nm, Raman scattering changes reflectivities by less than 4% according to Sromovsky (2005), and our correction was also smaller than 4%.

We determined the strengths of the main Raman transitions in the same way as Karkoschka (1998a), but allowed them to vary with μ . The strength of Raman scattering was roughly proportional to μ . We adopted this dependence, which is qualitatively expected since multiple scattering and path lengths of reflected photons increase toward the center of the disk. The same effect was detected in models of Neptune’s atmosphere by Sromovsky (2005, Figs. 18 and 21). For each of the ~ 7000 pixels on the disk of Uranus, we performed a full spectral calculation with our adopted parameters, which lead to Raman corrected reflectivities. The corrected spectra are fairly smooth shortward of 400 nm (cf. Fig. 7), where no significant methane bands exist.

We estimate that our imperfect correction for Raman scattering does not affect our main results, but may cause small systematic errors on results at weak methane absorptions of visible wavelengths, such as a minor offset in methane absorption coefficients or a systematic error in aerosol optical depths for the deepest levels probed in Uranus’ atmosphere.

Fig. 7 displays a correlation between reflectivity and Limb Darkening Ratio above 440 nm wavelength where methane absorption dominates. Beyond 540 nm (not shown in the figure), both curves remain remarkable similar with each detail in the methane absorption spectrum visible in both curves, except near 820 nm due to hydrogen absorption, which is consistent with theoretical expectations.

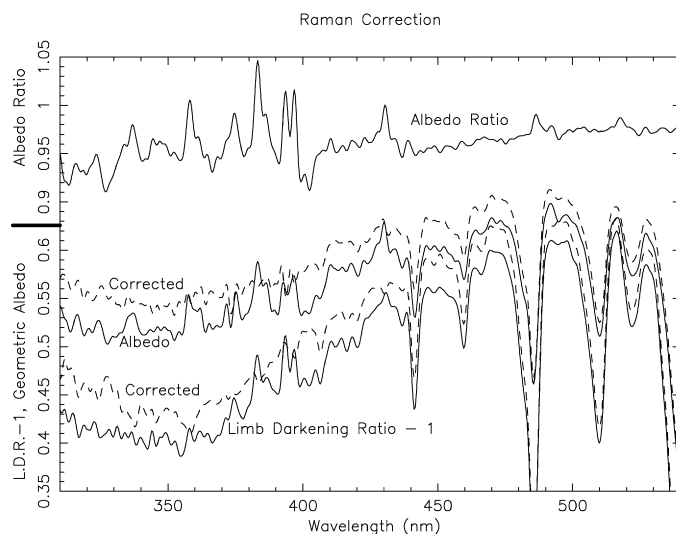


Fig. 7. The geometric albedo spectrum and the Limb Darkening Ratio (bottom solid curves). Raman corrected spectra are shown as dashed lines, which are much smoother at Fraunhofer lines. The ratio between uncorrected and corrected albedos is shown near the top. Beyond 540 nm wavelength, the ratio reaches 0.99 near 650 nm and then approaches unity.

2.11. Final sampling

We sampled Uranus in 1° latitude steps of 2° width between -84° and $+55^\circ$ latitude, which includes 99% of all pixels on the disk. This sampling preserved the spatial resolution, $\sim 3^\circ$ at the center of the disk, but was noisy at wavelengths of low signal. Six wider, representative latitude regions provided data of low noise (Table 2). Our latitudes are planetographic to simplify interpretations. For example, at the central meridian, emission angles differ from planetographic latitudes by the sub-earth latitude, which was -20° in 2002.

We reduced the spectral data of 1750 wavelengths to 80 spectral bands, which contained most of the information and still left sufficient redundancy to check consistency. The first 15 spectral bands were continuum wavelengths: 15-nm wide averages centered on the wavelengths 310–430 nm and six bands in methane windows up to 587 nm (cf. dots in Fig. 5, panel “C” of Fig. 8). In bands with a non-zero methane absorption coefficient, we extrapolated reflectivities to zero absorption using data near the minimum. We excluded methane windows at longer wavelengths since extrapolation was not reliable.

Another 55 spectral bands characterized eight methane bands (Table 2). We divided each methane band in 4–11 spectral bands, separated by a factor of two in the methane absorption coefficient (cf. panel “M” of Fig. 8). For each of the 55 spectral bands, the weighting of the ~ 20 contributing wavelengths was linear with wavelength, and the slope parameter of the weighting function was adjusted to provide the same mean wavelength for all spectral bands of the same methane band. Fig. 9 displays geo-

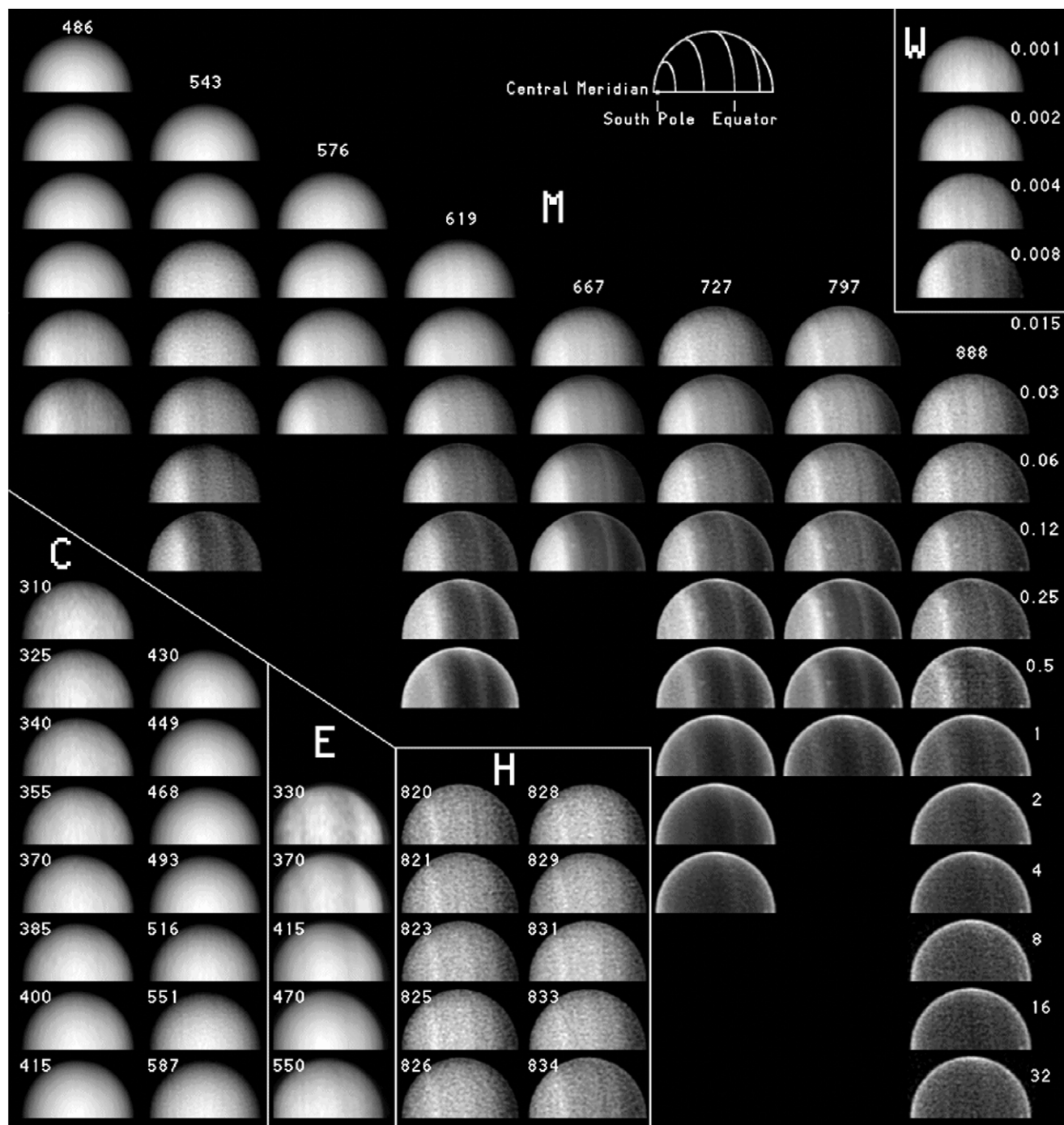


Fig. 8. Observations in our 80 spectral bands. The main panel “M” shows the 55 images in methane bands, ordered according to wavelength (left to right) and methane absorption coefficient (top to bottom). The four weakest methane absorptions, averaged in wavelength, are displayed with enhanced contrast in panel “W”. Near the bottom are continuum images “C”, with enhanced contrast “E”, and hydrogen absorption images “H”.

metric albedos averages where just one spectral sample of each side of the center of a methane band was averaged (dots) and where all (typically ~ 20) spectral samples within a factor of two in methane absorption coefficient were averaged (open circles).

Our method provided images at various methane absorption coefficients with the same effective wavelength, and images at various wavelengths with the same methane absorption coefficient. This eliminated the main intrinsic difficulty of previous data sets of distinguishing variations due to methane absorption from other variations with wavelength, such as aerosol optical depths or optical constants. This feature applies for seven of the

eight methane bands, since hydrogen absorption contributes in the 797-nm methane band.

The last 10 spectral bands covered the 819–835 nm region in 1.6-nm wide averages (panel “H” of Fig. 8), which include the strongest hydrogen absorptions. Altogether, most of the 1750 wavelengths were used in a single spectral band.

In summary, the final sampling reduced the whole three-dimensional data set of 12 million data points (7000 pixels on Uranus, 1750 wavelengths) to a set of 320 data points for each latitude, four reflectivities (I_2/F , I_4/F , I_6/F , and I_8/F) in 80 spectral bands. Within all 140 latitudes, six latitude regions characterized the basic latitudinal variations (cf. Table 2).

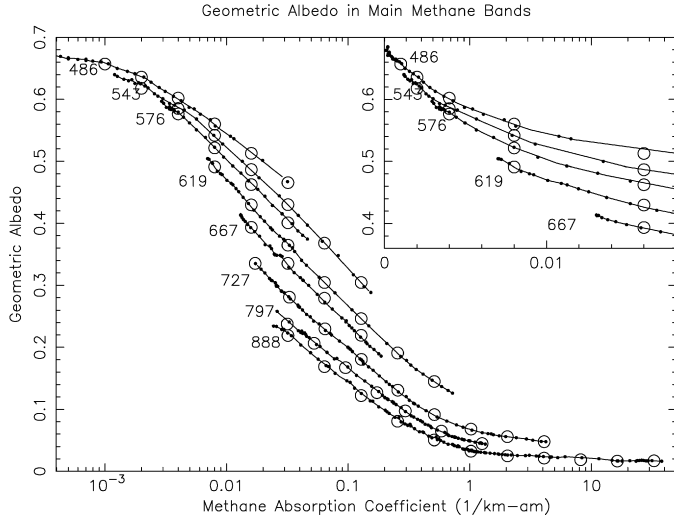


Fig. 9. Geometric albedo as functions of the methane absorption coefficient for eight methane bands. Dots are averages from one spectral sample each on both wings of the band. Curves connect these dots. The large open circles show our 55 representative spectral samples. The inset display has a linear instead of logarithmic horizontal axis. The 797-nm data was horizontally displaced to account for hydrogen absorption.

Fig. 9 gives a sensitive consistency test on small spectral scales between the STIS and ESO spectra. The latter defined the methane spectrum (Karkoschka, 1998a). Inconsistencies between both data sets could derive from telluric absorption bands, from spectral features in the CCD sensitivity such as fringes, and from calibration techniques. The ESO spectra were calibrated by a standard star, while the STIS data used a solar flux spectrum and the STScI flux calibration. All eight curves of Fig. 9 are smooth throughout to about 1%, indicating a good consistency.

3. Latitudinal structure

3.1. Opacity on Uranus

In order to interpret the latitudinal structure of Uranus, we first review the contributions of opacity and their vertical structures, so we can estimate the altitudes probed at different wavelengths. For the composition of the atmosphere, we used a 15:85 mixing ratio of helium to hydrogen from Conrath et al. (1987). The distribution of the third most abundant species, methane, is connected to the vertical temperature structure. Lindal et al. (1987) determined temperatures from Voyager occultation data. They assumed a constant methane relative humidity down to the 1.2 bar level and a constant methane mixing ratio at lower altitudes. Their structure had one unknown parameter, and possible models were labeled B, C, D, E, and F. Methane relative humidities for these five models were, 0, 0, 30, 45, and 53%, and methane mixing ratios were 0.011, 0.018, 0.023, 0.029, and 0.040, respectively. We based initial calculations on their favorite model D and then considered their other models and interpolations in between.

Using this methane mixing ratio profile, Fig. 10 (central panel) shows the cumulative optical depth of methane for a set of 13 methane absorption coefficients (Karkoschka, 1998a), separated by factors of two. The top 0.5 bar region of Uranus is transparent to methane, even for the strongest absorptions in our spectral range. The left panel of Fig. 10 shows the cumulative Rayleigh scattering optical depth. It is the dominant opacity at 300 nm wavelength, but 140 times smaller and thus negligible at 1000 nm. The right panel of Fig. 10 shows the absorption optical depth of equilibrium hydrogen at a few selected wavelengths near 820 nm, based on coefficients from Borysow and Fu (2000). This absorption is collision

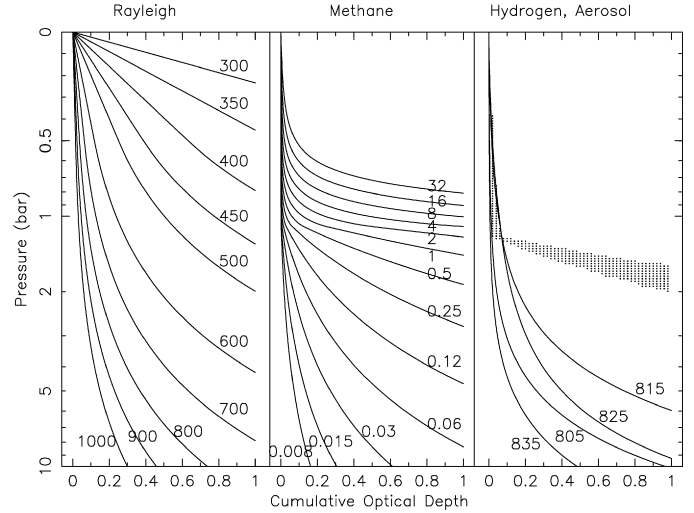


Fig. 10. The cumulative optical depth for Rayleigh scattering (left), methane absorption (middle), and hydrogen absorption (right) as function of pressure. In the left and right panels, wavelengths are labeled in nm. In the center panel, methane absorption coefficients are labeled in km-am^{-1} . The right panel also displays the haze optical depth (shaded). Note that the pressure scale changes from linear to logarithmic at 0.5 bars.

induced and thus proportional to the square of density, and also somewhat temperature dependent. On the same plot, the range of aerosol optical depth is also indicated (shaded area) as will be determined in Section 6.

Altogether, the top bar is quite transparent, aside from Rayleigh scattering in the ultraviolet. Between 1 and 2 bars, aerosols and methane compete, depending on the methane absorption coefficient. The narrow spacing of methane curves in this region makes methane absorption an accurate probe of specific altitudes. Below 2 bars, hydrogen contributes near 820 nm wavelength.

For the interpretation of the observations, we can change labels in Fig. 10. If we label the horizontal axis as μ , each curve shows the pressure level at which the optical depth becomes unity. It becomes obvious that for $\mu = 0.2$ one probes higher altitudes than for $\mu = 0.8$.

3.2. Lower atmosphere

Wavelengths with the smallest methane absorption coefficients probe the deepest levels on Uranus. While reflectivities at these wavelengths probe all altitudes down to the penetration level of light, ratios of reflectivities of similar wavelengths but slightly different methane absorption coefficients are particularly suitable to probe the deepest levels since light reflected from high altitudes is almost perfectly canceled out in the ratio. The main problem of probing the deepest layers is that their signal is very weak compared to the reflectivity. For example, if the ratio involves two reflectivities different by 1% due to slightly different absorption coefficients, this 1% signal from deep layers may be similar to the noise in the data. Thus, we designed a method to use all spectral data at small absorption coefficients, some 100 of more spectral points, and combined them in such a way to minimize noise without introducing systematic errors from spectral variations other than the methane absorption coefficient.

We start with the reflectivity as function of methane absorption coefficient κ and methane abundance along the path of light w if that abundance is the same for all photons:

$$\ln(I/F) = -w\kappa + \text{constant}. \quad (3)$$

For a set of observed reflectivities, the best estimation of the quantity w is a least square linear regression of $\ln(I/F)$ versus κ ,

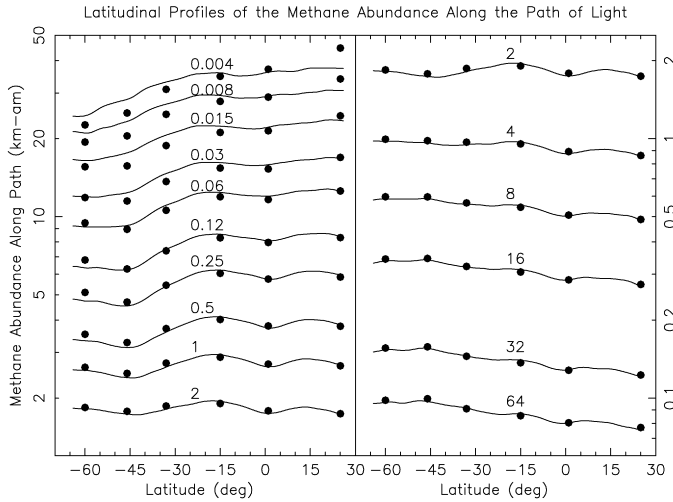


Fig. 11. Latitudinal profiles of the methane abundance along the path of light as defined in Section 3.2. Each of the 15 curves uses all reflectivities I_8/F with methane absorption coefficients up to the indicated number in km-am^{-1} . Solid dots are synthetic data from our final radiative transfer model. Relative uncertainties are about as large as the size of the solid dots, except for noise in the “0.004” curve.

which also provides the uncertainty of w using the uncertainty of each data point. For each methane band, we used all spectral samples up to a limiting methane absorption coefficient for this linear regression. We then averaged the obtained values of w from all methane bands with a weighting inversely proportional to the square of each uncertainty of w . This creates the best estimation of w from all spectral points with methane absorption coefficients between zero and the chosen limit.

Latitudinal profiles of this quantity are shown in Fig. 11 for reflectivities I_8/F and for 15 selected maximum methane absorption coefficients. If the atmosphere of Uranus were similar to a reflective layer model, Eq. (3) would hold and all 15 curves would plot on top of each other. In reality, this is far from true. Therefore, the curves are dependent on the selection of spectral points and can be only compared with model reflectivities put through the same method as the observed reflectivities. The quantity w determined with our method is a measure of the mean methane abundance along the path of light.

The curves of Fig. 11 allow a unique insight into deep layers of Uranus since few data sets allow measuring the variation of reflectivity with methane absorption coefficient using only coefficients smaller than 0.004 or 0.008 km-am^{-1} . On the other hand, the curves with the largest limits probe high altitudes, where the low mixing ratio of methane yields very low methane abundances along the path. A local maximum of w indicates a high probed methane mixing ratio or low aerosol opacity at that latitude. The methane abundances along the path range over a factor of 500. This indicates that the observable opacity in the atmosphere of Uranus is distributed over large ranges of altitudes. The smallest methane absorptions are uncertain since they have been barely detected in the laboratory. This could shift the curves of Fig. 11 somewhat without changing their shapes.

The curves in Fig. 11 with limits of 0.12 km-am^{-1} or larger have a structure known from methane bands images, considering that high reflectivity in images corresponds to low methane abundance along the path of light. The curves with lower limits yield new insights for deeper layers. They are difficult to probe since they require measuring reflectivity ratios between two similar wavelengths of very small but different methane absorption coefficients.

One intriguing feature is that the profiles probing deep layers, such as the 0.03 km-am^{-1} profile, show the structure familiar from Uranus images taken during the late 1990's, when the reflectivity

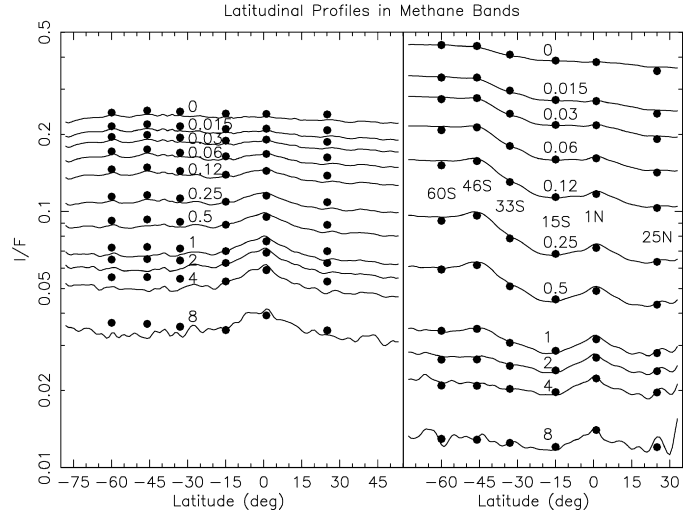


Fig. 12. Latitudinal profiles for wavelengths with methane absorption coefficients larger than the indicated values for reflectivities I_2/F (left panel) and I_6/F (right panel). Solid dots are synthetic data from our final radiative transfer model. Our six latitudinal regions are labeled at the right panel. Relative uncertainties are about as large as the size of the solid dots, except for noise in the bottom curves and within 5° of the both ends of each curve.

tivity south of -40° latitude was quite flat. Two curves down in Fig. 11 (0.12 km-am^{-1}), the profile is comparable to images taken around 2002. Two curves further down (0.5 km-am^{-1}), probing still higher altitudes, the profile is familiar from Uranus images taken around 2005. These images display a bright collar near -45° latitude, corresponding to the dip in the curves seen in Fig. 11. It seems that the structure at the lowest altitudes retains the memory of previous years, while the high-altitude structure predicts the future seen at intermediate layers. A possible explanation is that the aerosol opacity structure forms at relatively high altitudes. Then, the aerosols take a few years to fall to layers mostly probed by imaging. Another few years later, spectroscopic methods can still detect them at deep layers.

3.3. Upper atmosphere

We averaged reflectivities of all wavelengths with a certain minimum absorption coefficient to probe high altitudes. The left and right panels of Fig. 12 use the reflectivities I_2/F and I_6/F , respectively, for 11 selected minimum coefficients. Only curves near the bottom of Fig. 12 are noisy. In the middle of the right part, the latitudinal structure is familiar from the last plot, considering the contrast reversal between reflectivity and methane abundance along the path of light. Further down in the figure, which means higher in the atmosphere, the main feature is a bump centered on the equator. This feature at high altitude is best characterized in the left panel of Fig. 12, probing the highest altitudes. The feature is resolved since its width is wider than the width of the PSF ($4\text{--}8^\circ$ in latitude). However, the peak area has a similar shape as the PSF. Thus, in reality, the peak is probably very narrow and steep.

Using the data within 5° of the equator, we estimated the latitude of the peak. For the curves on the left panel of Fig. 12 between 0.25 and 4 km-am^{-1} , we get latitudes between 0.0 and -0.2° , while the peak moves just north of the equator for the curves further up. The curves on the right panel of Fig. 12 probe lower altitudes and give latitudes for the peak near 0.2° for the lowest three curves, getting consistently further north with each curve, until they reach 1.6° for the top three curves, probing still lower altitudes.

In the left panel, the limiting accuracy comes from an uncertainty of 0.2° for the effective latitude of each pixel near the limb.

In the right panel, the limiting accuracy comes from data noise which is about 0.3° for the lowest curves and less for curves further up. We conclude that at the top 1 bar, the feature peaks at latitude $0.0 \pm 0.2^\circ$, while curves probing all altitudes yield $1.6 \pm 0.2^\circ$. Thus, at lower altitudes the peak must be north of 1.6° .

What could create a feature, which has a very steep peak within 0.2° of the equator? Our first thought was an origin connected with ring material spiraling down onto the top of the atmosphere. We may not see the material itself, but the material may provide the seeds or the conditions for a more effective growth of aerosols than at other latitudes. The spread of $15\text{--}20^\circ$ in both directions may be due to diffusion. The shift of a few degrees north at lower altitudes may come from a meridional wind near the 1-bar level, taking the aerosols further north as they fall. This explanation is not completely satisfactory since we do not know a process which could transform the tiny influx from the ring into a major feature in the upper atmosphere of Uranus. The alternative explanation as a dynamic feature in the atmosphere is possible, but it seems hard to understand why such a narrowly peaked feature would form exactly at the equator.

Curves probing high altitudes in Fig. 12 show no other small-scale features above the noise level, but a gradual slope down from south to north, at least for northern latitudes, while southern latitudes seem almost perfectly leveled. This structure is similar to the insulation on Uranus in 2002, when the equator received as much solar energy as the south pole, diurnally averaged, with an almost flat distribution in between, but a relatively steep drop off to northern latitudes. Thus, the observed gradient may come from photochemically produced aerosols, with a high production rate in the southern hemisphere and a gradual drop off to the northern latitudes.

The increase of reflectivity from the 8 km-am^{-1} curves to the top curves derives from two reasons. First, less methane absorption gives larger reflectivities. Second, the lower methane absorption coefficients in the methane spectrum below 1000 nm wavelength are concentrated toward shorter wavelengths where Rayleigh scattering reflects more light. We separated both dependencies by assuming that reflectivity is a power law of methane absorption coefficient and of wavelength. We then found the two exponents for different latitudes with a least-square minimization, using the left-panel curves for absorption coefficients above 0.25 km-am^{-1} . For the equatorial bump, the exponents were -0.16 and -3.0 for the methane absorption coefficient and wavelength, respectively. Elsewhere, the exponents were -0.18 and -3.3 , respectively. At those latitudes, the reflectivity was slightly larger than expected from Rayleigh scattering alone. Models yielded exponents for a clear atmosphere of -0.15 and -3.5 , respectively. The former number comes from the methane column abundance growing almost with the seventh power of pressure around the 1-bar level (0.15 is about $1/7$). The wavelength exponent is close to the -4 power of the spectral Rayleigh scattering dependence in the limit of negligible aerosol optical depth. Thus, the vertical distribution of the aerosol opacity in the probed area and its wavelength dependence are both similar to those of the gas, which implies small particles roughly uniformly mixed with the gas. The -3.0 wavelength exponent for the equatorial bump may indicate a power law for the aerosol opacity alone with an exponent of -2.0 or -2.5 . Such a power law is typical for particles of around $0.2\text{ }\mu\text{m}$ radius.

The equatorial bump has been seen in many HST images and ground-based adaptive-optics images. The realization of its narrow nature and accurate equatorial placement required tedious navigational calibrations, which are not applied to every data set. The bump may be an impressive feature when imaged at much higher spatial resolution. Voyager 2 had the resolution, but no near-infrared imaging capability, where the feature is best seen. The

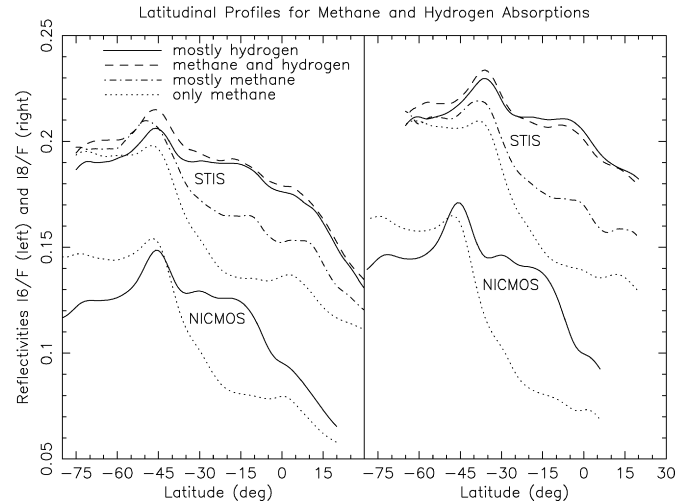


Fig. 13. Latitudinal profiles of the reflectivities I_6/F (left) and I_8/F (right) near the 820 nm hydrogen absorption. Wavelengths are ordered according to relative hydrogen to methane absorption coefficients. The four STIS curves are from our data set. The two NICMOS curves come from images in F095N (dotted) and F108N (solid) filters, taken in 1998. Relative reflectivities are accurate to 1–2%, which is much smaller than a tick mark, while the shape of the different curves varies by some 30%.

timing near solstice and the geometry of Voyager’s fly-by caused relatively poor imaging of the equator.

In summary, the albedo of Uranus at strong methane bands requires a minor amount of small aerosols above the 1-bar layer. These results are consistent with analysis from Voyager images by Rages et al. (1991) and Keck images by Sromovsky and Fry (2007). Aerosol optical depth decreases from the equator toward northern latitudes, but not to the south pole. On top of this structure is a significant, sharp equatorial bump.

3.4. Methane mixing ratio

In the $500\text{--}1000\text{ nm}$ spectral region, methane is the dominant absorber, except for the $818\text{--}832\text{ nm}$ region, where hydrogen absorption dominates through collision induced absorption. This region allows an important test. If latitudinal features in methane bands appear in hydrogen absorptions as well, they are due to aerosol opacity. If not, they are due to methane variations.

We used our 10 samples between 819 and 835 nm to separate hydrogen and methane absorptions. In Fig. 13, we divided them into four groups according to their relative methane to hydrogen absorption coefficients. Wavelengths with mostly hydrogen absorption show a roughly flat profile south of -10° latitude. Wavelengths with mostly methane absorption show a strong gradient between high and low southern latitudes. This suggests that methane and hydrogen absorptions are not well correlated, and that the methane mixing ratio varies with latitude.

Fig. 13 also shows profiles from HST/NICMOS images of 1998 (ID 7885, PI Hammel) in two stronger methane and hydrogen absorptions. These curves display similar features as the STIS data of 2002. The difference between methane and hydrogen absorptions is also prominent.

Unlike the NICMOS data with only two widely-spaced wavelengths, our 10 samples between 819 and 835 nm allow the separation between hydrogen and methane absorptions. At each latitude, we fitted the 10 data points by a function with three parameters, the continuum reflectivity and both gradients with respect to the hydrogen and methane absorption coefficient:

$$\ln(I/F) = -w_m \kappa_m - w_h \kappa_h + \text{constant}, \quad (4)$$

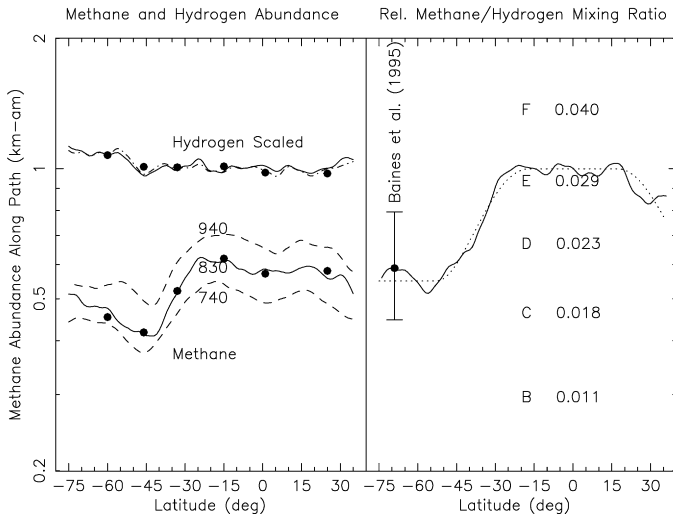


Fig. 14. The methane abundance along the path of light and an analog quantity for hydrogen for the 830 nm window (solid lines at left). Dashed curves are data for the 740 and 940 nm methane windows, and the dashed-dotted curve shows an alternative method for hydrogen. The normalized variation of the observed methane mixing ratio is shown at right (solid curve), and as adopted (dotted curve). Also indicated are the approximate levels for the models B, C, D, E, and F from Lindal et al. (1987) with their methane mixing ratios, and the level from Baines et al. (1995), plotted at the sub-earth latitude for their observations. Uncertainties in the left panel are similar to the size of the solid dots, which indicate radiative transfer calculations.

where κ_m and κ_h are methane and hydrogen absorption coefficients, and w_m , w_h , and the constant are the free parameters. For this fit, we chose 80 K as the temperature for hydrogen coefficients, based on radiative transfer models indicating average temperatures of levels probed by hydrogen absorption; other choices of temperature gave almost identical results. The results for parameters w_m and w_h are displayed in Fig. 14 (solid curves), similar to methane abundances along the path of light in Fig. 11. The hydrogen curve is scaled, because hydrogen absorptions coefficients have different units due to its dependence on the square of density as a collision induced absorption. Thus, only latitudinal gradients are important, not the vertical location in Fig. 14.

For comparison, Fig. 14 also displays parameter w_m using data from the 740 and 940 nm methane windows, which do not have significant hydrogen absorptions. All three methane curves are consistent, aside from a real offset due to varying Rayleigh scattering with wavelength. The methane curves are also similar to those of Fig. 11 at similar methane absorption depths.

Fig. 14 displays a different method for parameter w_h . The methane variation in the 830 nm window was inferred by interpolating the measured variations in the 740 and 940 nm windows, which then was applied to the 10 samples at 819–835 nm wavelength. The remaining reflectivity decrease must be due to hydrogen absorption (dotted-dashed), agreeing with the solid curve.

At both edges of the 819–835 nm interval, we found expected systematic deviations of the data from the linear fit of Eq. (4). We found good linear fits by decreasing the wavelength interval, and also by modifying the linear dependence into a more realistic curve of growth. Each case confirmed the shapes of the curves in Fig. 14.

Our final adopted methane profile as function of latitude was based on a least square fit of the whole data set with models described in Section 6.4 and with the methane mixing ratio as a free parameter as function of latitude. This provided the absolute calibration for the methane mixing ratio, while the shape of the profile was almost perfectly approximated with the somewhat crude method described here.

For all our shown results, we assumed equilibrium hydrogen based on the result by Baines et al. (1995). We also did calculations

with their lower limit of 85% equilibrium (i.e. 15% normal) hydrogen, which influenced our results by less than our uncertainties. Calculations with 50% equilibrium hydrogen show a global shift of our results toward lower aerosol opacities and lower methane mixing ratios, but do not influence results about latitudinal variations. This still assumes an equilibrium fraction constant with altitude and latitude. If this fraction has a large variation with latitude, then some of our results would need to be modified. However, such a variation would be easily detectable in our hydrogen absorption data, which is very smooth with latitude, unless it is compensated by another effect of equal magnitude but opposite sign.

The shallow gradients for methane and hydrogen in Fig. 14 south of -50° and north of -20° latitude are similar and thus derive from minor gradients of aerosol opacity. The strong gradient of methane in between has no analog in the hydrogen curve and thus derives from a variable methane to hydrogen mixing ratio. *This means that the primary latitudinal variation seen in methane absorptions is due to a variable methane mixing ratio and not due to a variable aerosol opacity.* This result was very surprising to us, since it contradicts the key assumption by most previous comparable investigations, that the methane mixing ratio is independent of latitude. Methane mixing ratios by Sromovsky and Fry (2008) indicated a possible variation with latitude in the same sense as our data, but their uncertainties were larger than the variation.

Interpretation of methane band imaging, which has been so successful on Jupiter and Saturn in constraining aerosol parameters, has fooled us on Uranus. Because this is a result of profound implications, we were very skeptical at first and tried to come up with systematic effects which may have produced this result, but our result remained firm. Initially, our work focused on the 98% of the wavelengths outside the 818–832 nm hydrogen absorption, which can be easily interpreted with constant methane. Inclusion of the last 2% of the wavelengths made us realize that common wisdom was wrong, and that we had to redo most of our work.

A rough estimation of the variability of methane mixing ratio with latitude follows here. We averaged the reflectivities between 825.4 and 827.4 nm wavelength, which probe mostly hydrogen absorptions. Then we looked for the wavelength of the matching reflectivity in the 833–835 nm region, where methane dominates. This gave us two data points with the same reflectivity, but different combinations of methane and hydrogen absorption coefficients. As a first approximation, the ratio of the absorption coefficient differences between both data points is proportional to the methane to hydrogen mixing ratio (Fig. 14, right). This method is exact if all latitudes probe to the same level, or if the vertical distribution of methane and hydrogen absorption is the same. Neither condition is accurately met at Uranus, so that Fig. 14 provides only an approximate latitudinal variation of methane. Fig. 14 suggests that low latitudes have roughly twice as much methane as high southern latitudes. This factor is an average factor over all probed altitudes, down to the ~ 2 bar level, and its variation with altitude is not constrained.

Our method includes a small correction, eliminating a systematic effect. Since wavelengths with the same methane absorption coefficient in the 740 and 940 nm methane windows show a gradual decrease of reflectivity with increasing wavelength, we selected the two data points discussed above with the same gradient.

Fig. 14 displays approximate levels for the models by Lindal et al. (1987), based on spectra calculated with radiative transfer calculations, which are only slightly dependent on assumed aerosol distribution. Lindal used data near the equator, and our data near the equator is most consistent with Lindal's model E, maybe slightly toward model F. At high southern latitudes, the data suggest models between C and D, but they could be very different too considering that these latitudes had no Voyager occultation data.

Baines et al. (1995) modeled spectroscopic data of hydrogen quadrupole and methane absorptions. They provided a nominal methane mixing ratio below the 1.2 bar level of 0.016 with an uncertainty interval between 0.011 and 0.023. Their spatially unresolved data probed mostly high southern latitudes, and our mixing ratios for these latitudes are similar (cf. Fig. 14). Their data plot a little higher than Lindal's for the same mixing ratio due to a higher assumed methane humidity (100%) above the 1.2 bar layer. Baines et al. (1995) assumed that their unresolved measurement would apply to all latitudes, but our result contradicts this assumption.

The variable methane/hydrogen mixing ratio implies that hydrogen is variable too. For example, if the methane mixing ratio increases from 0.015 at the equator to 0.03 at the pole, the hydrogen mixing ratio decreases by 1%, the gas density decreases by 8% (along isobars) due to increased mean molecular weight, and the gas density decreases another 6% due to the change of gravity, which adds up to about 14%. Thus, the 100% increase of methane/hydrogen mixing ratio corresponds to a 14% decrease of hydrogen density and a 71% increase of methane density. A 14% decrease of hydrogen density is almost a 28% decrease of hydrogen absorption, since the collision induced absorption is proportional to the square of density. Thus, the $\sim 10\%$ gradient of the hydrogen curve (left panel of Fig. 14) becomes a $\sim 20\%$ gradient of opposite sign when accounting for the variable hydrogen density. The south pole has stronger aerosol opacity than the equator, opposite to the first impression of the curve. All our calculations used appropriate hydrogen densities. They are based on a temperature profile independent of latitude. Major temperature variations with latitude would change hydrogen densities and thus hydrogen absorption, but none have been reported, nor are they expected.

3.5. Microwave temperature

Our latitudinal methane profile reminded us of results by Hofstadter and Butler (2003), who measured Uranus' effective brightness temperature at microwave wavelengths as function of latitude and time. The large contrast between warm high and cooler low southern latitudes was probably due to a microwave absorber such as ammonia concentrated at low latitudes. Our similar finding for methane may suggest a similar cause for the ammonia and methane profile.

We checked if the brightness temperature may be linearly correlated to the methane mixing ratio by linearly scaling our methane profile to the minima and maxima observed brightness temperatures. We accounted for the FWHM data listed by Hofstadter and Butler (2003) and simulated limb darkening. Some profiles agree fairly well (Fig. 15). The 2 cm data of 1994 agree with our simulated curve after a navigational offset of 0.01 arc-sec in the north-south direction on Uranus (east-west in the sky), which is within Hofstadter's quoted accuracy (0.01–0.02 arc-sec).

Since our simulated curves as function of time roughly match the observed ones, the apparent temporal variation of brightness temperature profiles may be an artifact of the varying spatial resolution and changing geometry. Thus, we disagree with Hofstadter's conclusion that the latitudinal structure of the microwave brightness temperature must have changed with time. More data may be needed to prove a temporal variability of an absorber such as ammonia, and our one-time STIS data cannot tell if there is a temporal variability of methane.

There is a offset in the location of the transition between low and high southern latitudes. The mid-way latitude is -35° in our data and -45° in the high-resolution microwave data of 1994. This 10° shift is far greater than navigational uncertainties. We have two explanations.

The microwave brightness temperature is probably not linearly correlated with the ammonia mixing ratio. The expected non-

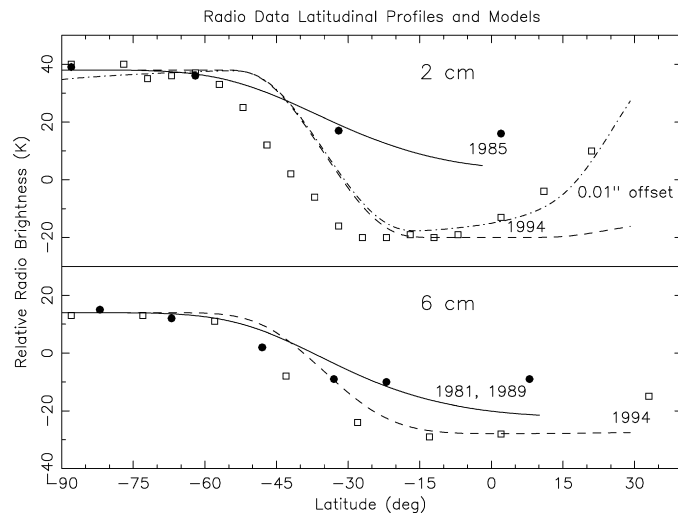


Fig. 15. Radio brightness data by Hofstadter and Butler (2003, symbols) at 2 cm (top) and 6 cm wavelength (bottom) and our methane mixing ratio (curves), scaled to fit minima and maxima. For the 1994 data at 2 cm wavelength, a corrected profile for a navigational error of 0.01 arc-sec is also shown (dashed-dotted). The apparent seasonal variation between the 1994 and earlier data is explained by the poorer spatial resolution of the earlier observations. The shift between both data sets at mid-southern latitudes is significant. Relative observational uncertainties are a few K except for the furthest data points to the right, which correspond to latitudes within one resolution element of the limb.

linearity has the correct sign to account for part of the shift. Future microwave models may tell if the shift could be 10° . Alternatively, ammonia or another absorber at deep levels may not be perfectly correlated with methane further up, which could yield insights in the workings of the atmosphere of Uranus. Even without explaining the shift, the correlation between very different data sets probing different levels is encouraging.

3.6. Continuum spectrum

The dots plotted in Fig. 5 confirm the well known continuum spectrum of Uranus. Ultraviolet absorption derives from aerosols high in the atmosphere. Toward 550 nm wavelength, this absorption becomes negligible as the albedo rises to levels consistent with conservatively scattering aerosols. Little is known about the single scattering albedo of aerosols longward of 550 nm. Baines et al. (1995) used the geometric albedo spectrum of Uranus to infer that absorption from H_2S may absorb longward of 600 nm. Our data set includes spatial information and allows a further analysis of aerosol absorption.

We estimated continuum albedos at the 551, 578, 633, and 678 nm methane windows. Extrapolation of our data to the continuum using methane absorption coefficients by Karkoschka (1998a) yields the open circles of Fig. 5, which may indicate some absorber if one ignores uncertainties of absorption coefficients. The laboratory measurements at room temperature by Fink et al. (1977) have the smallest uncertainties of 0.01 km-am^{-1} occurring in methane windows. The change in temperature to Uranus conditions causes a similar, additional uncertainty. At 700–1000 nm wavelengths, a change from zero to 0.01 km-am^{-1} methane absorption changes model reflectivities by up to a factor of two. Considering that our reflectivities are accurate to a few percent, the uncertainty by methane absorption coefficients is by far the major uncertainty in modeling data near methane windows. Uranus modeling has to include the methane absorption coefficient as a free parameter within its uncertainty. For example, in Fig. 5 we show the possibility that continuum reflectivities are constant between 550 and 700 nm (filled circles in Fig. 5). This corresponds to an increase of methane

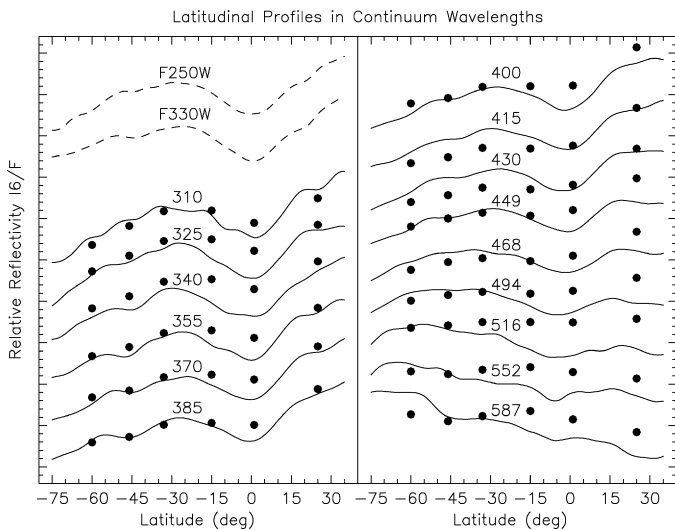


Fig. 16. Latitudinal profiles of the relative reflectivity in continuum wavelengths (solid curves). One small tick mark corresponds to 2% in reflectivity. Successive curves are shifted by one large tick marks, corresponding to 10% in reflectivity. Two ultraviolet filters from the 2003 ACS images are included for comparison (dashed curves). Relative uncertainties are about as large as the dots, which mark the final radiative transfer model. In the visible, imperfections of our model may indicate the presence of minor latitudinal variations of aerosol absorption.

coefficients by 0.0005, 0.002, 0.005, and 0.009 $\text{km}\cdot\text{am}^{-1}$ in these four windows, respectively, which is well within uncertainties.

The spatial information in our data gives us clues to decide between the different possibilities. When using Karkoschka's coefficients, the latitudinal structure of continuum reflectivities is remarkably similar to the structure seen in Fig. 11 for the weakest methane absorptions. This would imply a coincidence that the latitudinal variation of the aerosol absorption is the same as the combined latitudinal variation of methane mixing ratio and aerosol opacity. In the case of increased absorption coefficients as described above, the reflectivities are not only constant with wavelength, but their latitudinal variation also becomes almost flat.

Radiative transfer models described in Section 6 indicate that observed reflectivities at all methane windows between 700–1000 nm wavelength and all latitudes can be modeled with conservatively scattering aerosols, if methane absorption coefficients are increased by 0.01 $\text{km}\cdot\text{am}^{-1}$, similar to the increase at 678 nm, and also within their uncertainty. Thus, there is no evidence of aerosol absorption on Uranus in the 700–1000 nm region within current uncertainties.

However, if we used the vertical aerosol model by Baines et al. (1995), where no light reaches below the 3 bar level, we also needed darker aerosols. Thus, considering various model structures is important for interpreting albedos in methane windows. Note that Sromovsky and Fry (2007) also argued that light penetrates below the 3-bar layer, at least at longer wavelengths.

We researched the possibility of aerosol absorption in the 600–1000 nm region. We found good fits indicating that this possibility is consistent with our data. However, we needed aerosols with different single scattering spectra, smooth spectra at low latitudes, but a spectral absorption feature at 830 nm at high southern latitudes. This is an indication of a faulty model, since a faulty model would create features near 830 nm due to the different distribution of hydrogen and methane absorption. Thus, we conclude that aerosol absorption is probably small compared to methane absorption in the methane windows between 600 and 1000 nm wavelength.

Fig. 16 displays the latitudinal variations of reflectivity for our set of 15 continuum wavelengths. The featureless continuum appearance of Uranus at visible wavelengths is in stark contrast with

Jupiter and Saturn, which have a rich banding structure. This implies that latitudinal aerosol variations are subdued on Uranus.

At ultraviolet wavelengths, Uranus displayed an equatorial valley and a general gradient up from south to north. Both features appeared in methane bands with opposite contrast (cf. Fig. 12), a common anti-correlation due to aerosol opacity, which is dark compared to Rayleigh scattering in the ultraviolet, but bright compared to methane absorption.

In methane bands, the equatorial bump was much larger than the gradient, just opposite to the relative sizes in the ultraviolet. This suggests that the region above the 1-bar layer was not uniform. There were at least two kinds of aerosols with different ratios between ultraviolet absorption and near-infrared opacity. For example, stratospheric and tropospheric aerosols could have been different. More realistic is the haze model by Rages et al. (1991), which has aerosol sizes continuously changing with altitude as expected from cloud physics models, where small aerosols are created at high altitudes, which then grow by coagulation as they fall to lower levels.

4. Modeling technique

The results of Section 3 were obtained without running a single radiative transfer model, which can produce at least approximate results in many cases. Nevertheless, a validation should come through full-scale radiative transfer calculations. All results of Section 3 passed this test as described in the following three sections.

4.1. Radiative transfer code

We used two radiative transfer codes for the model calculations: one treats polarization of light accurately while the other one ignores polarization, but runs some 20 times faster. For most of our model search, we used the fast code by applying estimated offsets for the polarization effect, but all of our final results are based on the accurate code. Both codes use the doubling and adding technique for horizontal layers. The curvature of Uranus is insignificant since its atmospheric scale height is so much smaller than its radius. The codes allow for Rayleigh scattering, various aerosol scattering functions, and molecular absorptions in up to 30 different layers. Within each layer, mixing is assumed homogeneous. We tested the codes with a few standard cases where analytical results are known. The codes follow the shape of the phase function in the singly scattered light, and expand the azimuthal structure of the multiply scattered light by six Fourier coefficients. They use 11-point Gaussian integration in zenith angle for the upward and downward streaming radiation. Size distributions in Mie scattering calculations used 200 different sizes to smooth out structures of the phase function such as the rainbow or glory.

4.2. Methane mixing profile

For Uranus, we used the calculated gravity at each latitude, which varies between 8.7 and 9.2 m s^{-2} from equator to pole using the gravity field by French et al. (1988). Our equatorial methane mixing ratio profile is based on the standard models by Lindal et al. (1987), considering that the occultation experiment probed only equatorial latitudes. The comparison between methane and hydrogen absorptions of Fig. 14 suggests that Lindal's model E or an average between models E and F is most appropriate. Thus, we adopted an equatorial methane mixing ratio of 0.032 below the 1.2 bar level and a relative humidity of 48% at the 1.15 bar level. Lindal et al. assumed a constant humidity further up, although their data loses sensitivity to methane near 0.7 bars. We tested this assumption.

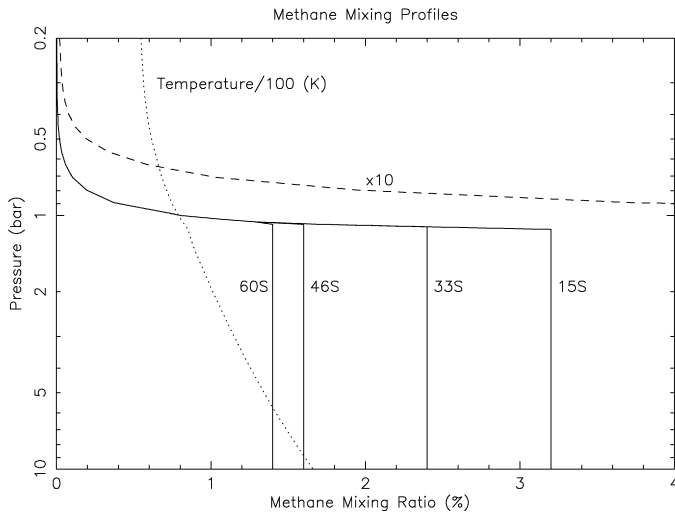


Fig. 17. The adopted methane mixing ratio as function of pressure level for four latitude regions (solid curves) and on a 10 times magnified scale (dashed). The temperature profile scaled down by a factor of 100 is displayed as the dotted line.

For a constant relative humidity, our deep methane band data require significantly higher aerosol opacity in the 0–0.5 bar region than in the 0.5–1 bar region, which contradicts cloud physics calculations (Rages et al., 1991), suggesting a more even distribution of aerosol opacity. We adopted a modified methane humidity, which then allows more evenly distributed opacity. Our humidity above the 1-bar layer is $RH = 48\%[1 - (1 - P)^2]$, where P is the pressure in bars. This variation leaves the humidity very close to 48% near 1 bar, consistent with Lindal’s data, but reduces it five times at the tropopause (~ 0.1 bars). This low humidity is roughly in line with other estimations for the stratosphere (Moses et al., 1995). If the humidity variation with altitude were different, it would slightly modify our inferred distribution of opacity above the 1 bar layer.

The same methane structure works well for all latitudes within 20° of the equator. Higher northern latitudes were only visible near the limb, which gives only weak constraints on methane. Higher southern latitudes have a strongly reduced methane mixing ratio as discussed in Section 3.4. Because our data set includes only weak hydrogen absorptions, we cannot determine the altitudes of reduced methane. However, the latitudinal profiles at methane absorptions give a hint (Fig. 11). The structure of bright polar latitudes and darker equatorial latitudes, indicative of reduced methane at high latitudes, is present for all weak methane absorptions, but disappears at stronger absorptions probing higher than the 1 bar level. *Thus, at high levels, methane may be uniformly mixed with latitude. The simplest way to modify the vertical mixing structure at higher latitudes is to cap the methane mixing ratio at a value depending on the latitude, and this is our nominal model.* Fig 14 (dotted curve) displays our adopted methane structure with latitude. The cap is 0.032 within 20° of the equator, 0.014 at latitudes south of -50° latitude, and it follows a sine curve in between: $0.023 + 0.009 \sin 6(\varphi + 35^\circ)$ where φ is the latitude. Our adopted methane mixing ratio as function of pressure level is shown for four latitudes in Fig. 17.

Even in the weak methane bands, most of the reflected light does not penetrate below the 2 bar level. *Thus, our latitudinal methane variation is well constrained in the 1–2 bar region, but less so at lower levels.* Our data allow the methane mixing ratio to be 0.032 at all latitudes below the 3 bar level, but they do not allow such a jump at 2 bars. A transition between 2 and 3 bars would require a minor decrease of mixing ratios at high latitudes between 1.2 and 2 bars. Theoretical expectations give a constant methane mixing

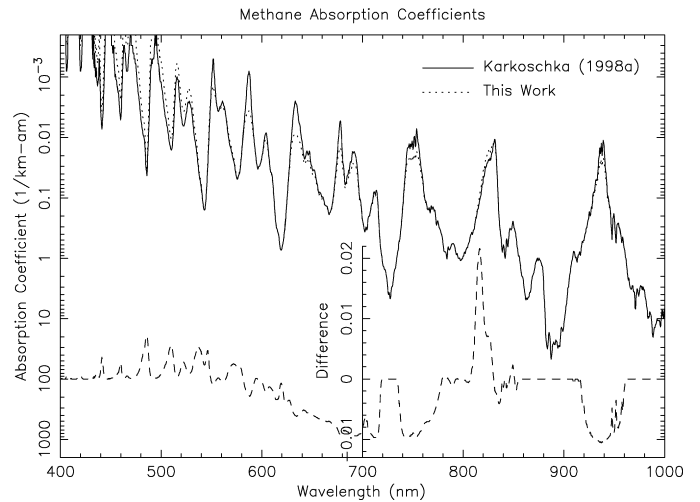


Fig. 18. Methane absorption coefficients from Karkoschka (1998a, solid curve) and the adjusted coefficients for this work (dotted curve). The difference between both coefficients is shown as the dashed curve on the linear scale inside. Almost everywhere, the difference is smaller than 0.01 km-am^{-1} .

ratio somewhere deep in the atmosphere. Our result is that this may be happening at the 3 bar level or at some deeper level.

4.3. Methane absorption coefficients

We used methane absorption coefficients by Karkoschka (1998a), except for three small corrections. The first one was discussed in Section 3.6. It increased the coefficients by up to 0.01 km-am^{-1} , mostly at near-infrared methane windows. The second correction was a decrease of coefficients of 0.007 km-am^{-1} for coefficients of 0.05 km-am^{-1} , going smoothly to zero change toward lower and higher coefficients. This change allowed simpler models.

The third correction was a small decrease near 820 nm wavelength. Our modeling of the hydrogen absorption required accurate methane absorption coefficients on both wings of the 830 nm methane window. This was not perfect in Karkoschka (1998a) since the shape of the methane spectrum was inferred from spectra of Jupiter, Saturn, and Titan. An accurate comparison of spectra allowed us to detect a small signature of the hydrogen absorption in the spectra of Jupiter and Saturn. We estimated its magnitude based on Titan’s spectrum (Titan has negligible hydrogen) and corrected for it. Fig. 18 displays the adopted methane absorption coefficients.

Banfield et al. (1998) adjusted the Karkoschka (1998a) coefficients to model Galileo data of Jupiter. For the 727 nm filter, they adopted a coefficient smaller by 10%, which they suggest may be due to Jupiter being warmer than the other giant planets, considering that coefficients are expected to be anti-correlated with temperature at this wavelength. In the 756 nm continuum filter, they adopted coefficients increased by a factor of 10, far more than the factor of ~ 1.5 increase suggested here, but noted that part or all of this absorption could derive from absorption in Jovian aerosols. Uranus albedos can rule out a factor of 10 increase by a wide margin.

The Karkoschka (1998a) coefficients were tested by data recorded by the spectrometers of the Descent Imager/Spectral Radiometer aboard the Huygens probe, as Huygens descended to the surface on Titan in 2005. The main result was that below 830 nm wavelength, the new data was consistent with the 1998 coefficients, but at wavelengths between 830 and 1000 nm, coefficients needed to be decreased by up to 30% to explain the observations (Tomasko et al., 2008). This inconsistency applied only to Huygens

data taken at high altitudes, but not for spectra taken at Titan's surface with illumination by a lamp. This indicates a pressure dependence. On Uranus, methane bands form at pressures about two orders of magnitudes higher than on Titan, so that this uncertainty should be minimal for Uranus. Methane bands form at similar temperatures at Titan and Uranus, although the tropopause temperatures are different. Thus, temperature dependency is not important for this comparison.

The Huygens data constrained the methane absorption coefficients in methane windows. With 1 km-am^{-1} of methane in Titan's lower troposphere and an assumed accuracy of reflectivities of 2%, the coefficients in methane windows are good to 0.02 km-am^{-1} . Our adopted offset of 0.01 km-am^{-1} is within this constraint.

In summary, there are no indications that our methane absorption coefficients have serious systematic flaws for the application to Uranus, but minor systematic effects could have escaped detection. We remain careful whenever results depend on methane coefficients. Most of our results involve latitudinal variations, where knowledge of methane coefficients is not critical. We used Beer's law for all methane absorptions since we found it to be a good approximation for our spectral resolution (1 nm) and the pressures where the bands form (~ 0.5 bars and more).

5. Aerosol properties

In this work, we separate the discussion of aerosol properties from that of aerosol distribution (Section 6). In reality, both are closely related. One cannot determine aerosol properties without the aerosol distribution, and vice versa. Both needed to be determined iteratively, which converges fast in the case of Uranus since aerosol distribution is mostly determined by methane bands, while aerosol properties are mostly determined by continuum data.

Our model assumed that Uranus had two kinds of aerosols, stratospheric aerosols above the tropopause, and tropospheric ones below. Aerosols at all latitudes were assumed identical. This very simple model gave good fits to all our data. If we had simplified the model to only one type of aerosol, the limb darkening observed at ultraviolet wavelengths would have required more stratospheric aerosol opacity than upper limits based on near-infrared reflectivities. Thus, stratospheric aerosol opacity decreased significantly with increasing wavelength, which indicated aerosols smaller than the wavelength. On the other hand, methane band data probing tropospheric levels were inconsistent with this wavelength dependence, but indicated opacities roughly constant with wavelength. Therefore, most tropospheric aerosols were at least as large as the wavelength, and thus different from stratospheric aerosols.

We modeled stratospheric aerosols with Mie scattering calculations according to spherical aerosols, and with fractal aggregates according to West (1991). Since our data could not distinguish between both kinds of aerosols we adopted the simpler Mie theory. We found fits for mean aerosol radii within a factor of two of $0.1 \text{ }\mu\text{m}$, our adopted size. This is similar to radii of $0.13 \text{ }\mu\text{m}$ at the tropopause and $0.10 \text{ }\mu\text{m}$ one scale height higher in the microphysical model by Rages et al. (1991). Pryor et al. (1997) analyzed Voyager ultraviolet data and found agreement with Rages' sizes. They could exclude sizes more than 20% larger than that.

We used a Hansen (1971) size distribution with a mean size $a = 0.1 \text{ }\mu\text{m}$ and a normalized size variance of $b = 0.3$, which is the variance divided by the square of the mean size. Such a wide size distribution minimizes sharp features in Mie phase functions. We fixed the real refractive index at 1.4. Smaller and larger indices produced identical results, as long as the imaginary index was adjusted.

Our data were quite sensitive to the imaginary index. It was large in the ultraviolet to produce sufficient absorption but orders

Table 3

Aerosol parameters as function of wavelength.^a

λ	Q	n_i	ω_s	ω_t	f_1
310	1.35	0.0821	0.639	0.730	0.470
370	0.99	0.0450	0.746	0.905	0.492
430	0.72	0.0247	0.829	0.978	0.544
516	0.46	0.0105	0.907	0.998	0.651
633	0.27	0.0032	0.961	1.000	0.803
740	0.18	0.0011	0.983	1.000	0.896
830	0.13	0.0005	0.992	1.000	0.931
940	0.09	0.0002	0.997	1.000	0.940

^a Listed are wavelength (nm), scattering efficiency and imaginary refractive index of stratospheric aerosols, single scattering albedos of stratospheric and tropospheric aerosols, and the weighting parameter for the Henyey Greenstein functions of tropospheric aerosols.

Table 4

Haze model.

Stratosphere: spherical aerosols of $0.1 \text{ }\mu\text{m}$ mean radius, size distribution with 0.3 normalized variance, refractive index $1.4 + n_i i$, cf. Eq. (5) and Table 3.

Troposphere: single scattering albedo, cf. Eq. (6) and Table 3, Henyey–Greenstein phase function with $g_1 = 0.7$ and $g_2 = -0.3$, f_1 , cf. Eq. (7) and Table 3.

Optical depths for four pressure regions: 0–0.1 bars (stratosphere), 0.1–1.2 bars, 1.2–2 bars, 2 bars– ∞ , cf. Fig. 21.

of magnitude smaller in the visible. An exponential dependence of the index as function of wavelength has been suggested for other planets, and it worked for Uranus. Small but consistent deviations at some continuum wavelengths, for example at 400 nm, do not necessarily require deviations from the exponential dependence since they are within the absolute calibration uncertainty. Both parameters of the exponential function were well constrained by our data if other parameters remained constant. Observations constrain mostly the aerosol absorption. The conversion between aerosol absorption and imaginary index depends on aerosol optical depth, aerosol size, and real refractive index, none of which is perfectly known. Thus, our adopted spectral dependence of the imaginary index n_i worked for our set of parameters, but it was not absolutely constrained:

$$n_i(\lambda) = 0.055 \exp[(350 - \lambda)/100], \quad (5)$$

where λ is the wavelength in nm. Our values (cf. Table 3) are similar to those in Rages et al. (1991) in the visible, but about three times larger in the ultraviolet. They quoted an uncertainty of a factor of three, similar to our uncertainty.

For tropospheric aerosols, our data constrained two parameters, the aerosol single scattering albedo from the reflectivity data, and the phase function at 180° scattering angle from observed limb darkening. Mie scattering phase functions often do not approximate the constraints from planetary space probes. A few schemes available for phase functions of non-spherical particles have too many free parameters to be constrained by our data. Thus, we adopted the simple scheme of phase functions by Henyey and Greenstein (1941). We used double Henyey Greenstein functions, which have four free parameters, the single scattering albedo, the average cosines of the scattering angle for both components, g_1 and g_2 , and the weighting (f_1 for g_1).

Our observations require the single scattering albedo of tropospheric aerosols to be quite low at ultraviolet wavelengths and then smoothly turn to unity in green light ($\sim 550 \text{ nm}$). Toward the near-infrared, it may stay near unity as discussed in Section 3.6. We adopted the spectral dependence for the single scattering albedo of

$$\omega_t(\lambda) = 1 - 1/[2 + \exp[(\lambda - 290)/37]]. \quad (6)$$

We adopted $g_1 = 0.7$ and $g_2 = -0.3$, which are typical parameters used for aerosols of the giant planets (Table 4). Our observed

limb darkening at continuum wavelengths indicated a significant backscattering of aerosols at ultraviolet wavelengths, but not in the near-infrared, with the transition occurring mostly in the visible. In order to fit our data, we adopted the weighting of

$$f_1(\lambda) = 0.94 - 0.47 \sin^4[(1000 - \lambda)/445]. \quad (7)$$

Both wavelength dependent parameters are listed in Table 3. The adopted phase functions are only a guess since our observations were quite sensitive to the phase function at 180° scattering angle, but not very sensitive to the rest of the phase function. For most particles, phase functions become steeper at small scattering angles toward shorter wavelength, corresponding to an increase of the parameter g_1 , but we left g_1 constant since we could not constrain its spectral dependence.

Our model with only one kind of tropospheric aerosols is the simplest one consistent with our observations. At short wavelengths, our observed limb darkening could also be explained by bright aerosols overlying dark aerosols with no backscatter. Such a model would have many free parameters that cannot be constrained, and thus we did not follow this path.

For tropospheric aerosols, we assumed that the optical depth is independent of wavelength, which is an approximation for particles larger than the wavelength. A minor variation of optical depth with wavelength could be compensated by a slight modification of Eqs. (6)–(7). A large variation with wavelength, such as the optical depth proportional to λ^{-2} , did not seem to produce simultaneous fits at short and long wavelengths.

Model intensities are most sensitive to aerosol parameters where the cumulative aerosol optical depth reaches the order of 0.1–1. Aerosols at higher altitudes do not contribute significantly to observed reflectivities in continuum wavelengths, where aerosol properties are best determined. Aerosols at lower altitudes mostly contribute light through multiple scattering, where the details of the phase functions do not matter much. On Uranus, cumulative optical depth between 0.1 and 1 is reached at pressure levels around 1.2–2 bars. Our data probed single scattering albedos and the phase function backscattering of aerosols at these altitudes. We adopted the same aerosol properties for aerosols at higher and lower altitudes, because we could not determine them independently. A vertical variation of aerosol type could slightly modify some of our determined parameters, but none of our main results.

6. Vertical aerosol structure

The observational constraints on the vertical aerosol structure in the atmosphere of Uranus have been so sparse that it was impossible to constrain the structure based on observations alone. Therefore, previous efforts started with some basic assumptions about the atmosphere, and then constrained some parameters within the assumed framework. A typical framework was a stratospheric haze and a few (mostly two) condensation clouds in the troposphere where species are expected to condense, methane near the 1.4 bar level and possibly H_2S about a scale height deeper (i.e. Rages et al., 1991; Baines et al., 1995; Sromovsky and Fry, 2007, 2008). Such an approach was successful for modeling the vertical structure of Jupiter where far more data exist. On the other hand, Irwin et al. (2007) started with a smooth opacity structure and used an iterative method to modify the structure until model and observations were consistent. Their final structure was still quite smooth with some concentrations at specific levels.

The data of this work offer the ability to test previous assumptions about the vertical aerosol structure. For this part of the work, we only show the data from the 888 nm methane band, which consist of 11 spectral samples ranging from the methane window to the bottom of the band. A similar investigation with

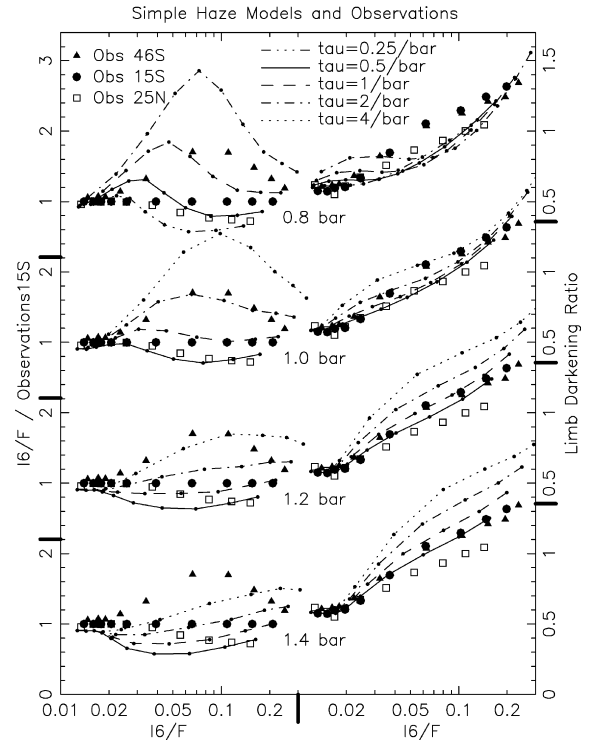


Fig. 19. Comparison of haze models (curves) with observations (symbols) in the 888 nm methane band. The left panels display reflectivities, normalized to the observations at 15S. The right panels display Limb Darkening Ratios. The listed pressure levels mark the boundary between clear gas (above) and haze uniformly mixed with gas (below), with haze optical depths per bar listed for each line type.

the 727 nm methane band produced similar, but slightly less constraining results. We used conservatively scattering aerosols and a vertical structure with a few free parameters specifying pressure levels and/or aerosol optical depths.

We fixed the aerosol properties as discussed in the previous section. Radiative transfer models with other aerosol properties supported our qualitative results of this section, but not the absolute values of optical depths. For example, a phase function with a steeper forward scattering peak gave similar fits with larger optical depths everywhere (such as twice as large), but left results on relative latitudinal and vertical distribution of optical depths unchanged.

6.1. Haze models

We start with the discussion of two-parameter models since the observations could easily contradict one-parameter models. The first free parameter was the pressure level that divided haze and clear gas. The structure was clear gas on top and haze uniformly mixed with gas below the pressure level, since the opposite case was easily eliminated. The second free parameter was the haze optical depth per pressure difference of 1 bar. Fig. 19 displays various combinations of the two free parameters (curves) with scaled observed reflectivities at three selected latitudes (left) and the observed Limb Darkening Ratios (right). On the left panels, the 11 data points are ordered from the 888 nm band center to the methane window. On the right panels, limb darkening is plotted as function of reflectivity. This makes the plot independent of methane absorption coefficients, since different coefficients would move data points along the curve, but would not change the curve at all. While uncertainties of methane absorption coefficients have been a major obstacle in the interpretation of methane band data, our data set allows some analysis of methane band data without knowledge about methane absorption coefficients.

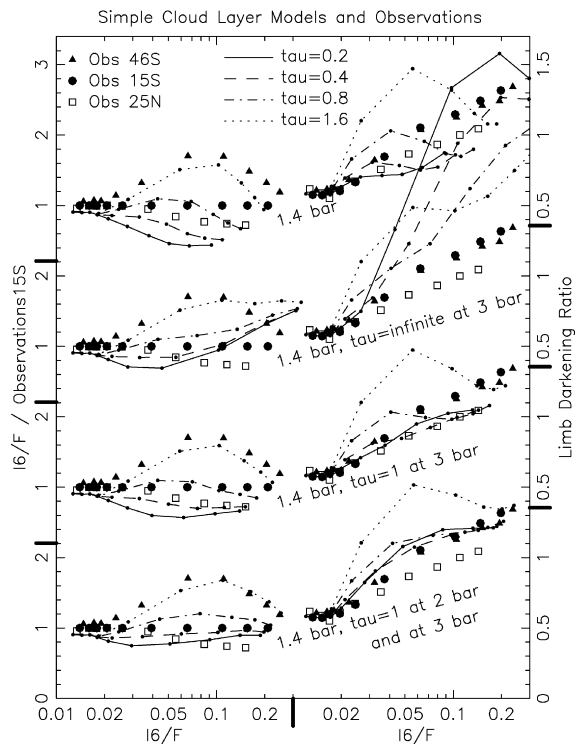


Fig. 20. Comparison of cloud layer models (curves) with observations (symbols) in the 888 nm methane band. The layout is similar to Fig. 19. The models have clear gas with a thin cloud layer at 1.4 bar pressure with an optical depth as indicated by the line type. The second panel from the top has an additional cloud layer of infinite optical depth at 3 bars. In the next panel, this optical depth is reduced to unity. In the bottom panel, another cloud layer at 2 bar pressure is added.

In Fig. 19, the panels from top to bottom have different pressure levels, while the haze optical depth is varied within each panel. Models with a pressure level of 1.2 bars and a haze optical depth between 0.5 and 2 bar fit reflectivity and limb darkening quite well. Models with a pressure level at higher altitudes were too bright deep in the methane band and too dark toward the methane window. Models with a pressure level lower in the atmosphere were too dark, unless the optical depth was so large that the limb darkening went far off the data.

The curves of Fig. 19 used a methane mixing ratio in the lower atmosphere of 0.023. The curves are really only sensitive to the ratio of methane mixing ratio and aerosol optical depth since Rayleigh scattering is very low at 888 nm wavelength. Thus, the latitudinal variations in the best fitting optical depths by roughly a factor of two suggested by Fig. 19 could also be due to a factor-of-two variation in the methane mixing ratio, or a combination of both. In Section 3.4 we learned that the latitudinal variation is mostly due to methane.

6.2. Cloud layer models

We investigated cloud layer models, which had the opacity concentrated at one or more pressure levels. Each layer had two free parameters, the pressure level and the cloud optical depth, unless the optical depth of the bottom layer was infinite, which we did not count as a free parameter. We did not investigate models with extended cloud layers since this would have only added free parameters without significantly changing results.

Fig. 20 displays some results for cloud layer models in a similar display as Fig. 19. The top panels show four examples for a cloud layer at 1.4 bars, which was the best choice, but still provided only poor fits. Cloud layer models with two layers fit better, with 3 bars being the best choice for the pressure level of the lower

cloud. A lower cloud with infinite optical depth did not fit observed limb darkening (second panel). Reducing the optical depth to about unity improved the fit for limb darkening (third panel). Nevertheless, all models with two cloud layers bright enough to fit reflectivities did not have the flat gradient observed for the limb darkening. This feature could be smoothed out by introducing another cloud at 2 bars (bottom panel). Instead of introducing a third cloud layer, one can improve the fit for a two-cloud model by adjusting single scattering albedo and phase function for each cloud layer individually. This model has a similar number of free parameters as a three-cloud model with identical aerosols.

Our data probe three different altitude regimes below the 1.2 bar layer, separated by about half a scale height, which is the vertical resolution of radiative transfer methods. Our data require opacity in each of those three regimes, which a haze model achieves with two parameters, but a cloud layer model only with six parameters. Cloud layer models with fewer parameters have features in the limb darkening curve (Fig. 20, right) while the data are smooth. Our data can exclude a significant cloud layer at the methane condensation level of 1.2 bars. This result is consistent with Sromovsky and Fry (2007), who first found this unexpected result.

We add a little insight, how the curves on the right panels of Figs. 19 and 20 are connected with the vertical aerosol structure. The left end of the curve probes high altitudes, where the data suggest a clear or almost clear atmosphere. Data points further right probe deeper and deeper levels. Where the data points start to climb, aerosol opacity appears near the center of the disk, where observations probe the deepest level, which increases the limb darkening ratio. Further to the right, the same aerosol opacity now appears close to the limb, which alone would decrease the limb darkening ratio. The fact that the limb darkening keeps climbing indicates that the center of the disk encounters more and more aerosol opacity. To the level of vertical resolution of the data, there is no evidence for a clear space or local increase of opacity.

Our research indicates that, assuming a cloud layer structure with two clouds for Uranus, the pressure levels of both clouds need to be around 1.4 and 3 bars, although the level of the lower cloud is less certain and very dependent on adopted methane mixing ratios and absorption coefficients. These levels are roughly consistent with Rages et al. (1991) and Baines et al. (1995). Note that their models were based on spatially unresolved data or imaging data with only one or two filters per methane band. With only one or two data points one cannot determine the shape of curves in Figs. 19 and 20, which we needed to distinguish between haze and cloud layer models. Thus, our results are consistent with previous results considering that our combination of high spatial and spectral resolution allowed improved vertical sampling of aerosols.

Our trial model with two cloud layers is less consistent with models by Sromovsky and Fry (2007, 2008) and Irwin et al. (2007), which had clouds near the 2–3 and 6–8 bar levels. These investigations used methane absorption coefficients by Irwin et al. (2006), which the Huygens data found to be significantly off for the conditions in Titan's atmosphere (Tomasko et al., 2008). In particular, weak coefficients were 3–5 times stronger than Irwin's. Using coefficients ~ 3 times too small would place the opacity on Uranus at three times the methane column abundance, e.g. at 2.5 bars instead of 1.5 bars, and 7 bars instead of 3 bars. This possible interpretation would make opacity levels of all investigations roughly consistent with each other.

Sromovsky and Fry (2008) suggested that Irwin's coefficients are suitable to accurately infer opacity on Uranus above the 1 bar layer, but become increasingly uncertain below the 1 bar layer due to large extrapolations needed from the laboratory conditions. Sromovsky et al. (2006) and Sromovsky and Fry (2008) also could accurately fit spectra of Uranus using Irwin's coefficients. This may suggest that coefficients could be valid for Uranus, unless they are

off systematically so that all coefficients of the same value are off by a similar amount. This occurs for Titan according to the Huygens data. Thus, a similar offset could occur for Uranus, and it could be larger or smaller than for Titan.

There is good agreement in the qualitative latitudinal variations of opacity between our work, [Sromovsky and Fry \(2007, 2008\)](#), and [Irwin et al. \(2007\)](#). For example, we all agree that the origin of the north-south asymmetry is deeper than the origin of the South Collar near -45° latitude. Our latitudinal variations may be less biased since our three-dimensional data allow viewing different latitudes at the same scattering geometries, while the other two investigations used spectroscopy along the central meridian, which required assumptions about the center-to-limb variation in order to retrieve latitudinal variations. This may be a minor difficulty for [Sromovsky and Fry \(2008\)](#) who focused their analysis on latitudes far away from the limb. This may be a major difficulty for [Irwin et al. \(2007\)](#) who included latitudes close to the limb, as close as 0.06 arc-sec, even though they used a wide slit (0.48 arc-sec) but not adaptive optics, and they did not mention latitudinal smearing due to limited resolution.

6.3. Discussion

[Lindal et al. \(1987\)](#) found a structure in the molecular weight near 1.2 bars, which can be interpreted as a methane condensation cloud, but [Sromovsky and Fry \(2007\)](#) found no cloud near that level. A similar situation appeared with Titan. Huygens found a dark layer at 21 km altitude ([Tomasko et al., 2005](#)) where the methane humidity was close to 100%. The layer with its vertical absorption optical depth of 0.001 was only detectable looking in the horizontal direction, similar to Lindal's Voyager occultation data. Observations from Earth do not have the sensitivity to detect a layer as optically thin as the 21-km layer on Titan.

If opacity on Uranus comes from condensation clouds, methane should be the primary candidate since it is by far the most abundant species for condensation. However, the methane condensation level does not have a significant cloud, which makes it questionable whether other species could produce cloud layers. Our data do not provide any evidence for a cloud layer.

With condensation clouds being unlikely candidates for the observed opacity, *the opacity may come from a vertically extended haze layer*. Considering that altitudes above the 1.2 bar level are almost clear, the region of aerosol production is probably near 1.2 bars, and the aerosols fall down from there. The fact that the methane condensation level is also at 1.2 bars may not be a coincidence. On Titan, aerosols grow significantly at altitudes of 100% methane humidity. On Uranus, aerosols may grow by a large factor at the 1.2 bar level. A three-fold increase in aerosol radius can increase the near-infrared aerosol opacity by up to a factor of 81.

Section 3.2 noted that the latitudinal aerosol distribution at lower levels seems to be delayed in time with respect to the aerosol distribution at higher altitudes. A model with distinct cloud layers cannot easily explain this observation, but the haze model provides this property, since aerosols are slowly falling to lower altitudes. This feature allows predictions about the aerosol structure, which can be directly tested by future observations. So far, observed temporal changes were not understood sufficiently well to allow predictions.

Temporal variations observed for the tropospheric opacity suggest a correlation with insolation and a seasonal phase lag of a few years ([Rages et al., 2007](#)). The phase lag may indicate the falling time from the haze production at the 1.2 bar level to the average probed altitudes. The correlation with insolation may indicate photochemical aerosol production. The 1.2 bar layer seems very deep for photochemistry, but the unique, almost clear atmosphere above this layer allows relatively deep penetration of sunlight.

Another clue, that Uranus' opacity below the 1.2 bar layer may be due to haze, comes from the time scale of aerosol opacity changes. The general latitudinal structure of our data set was still comparable with the structure Voyager saw 16 years earlier, although gradual changes from year to year have been recorded. This is consistent with time scales of falling aerosols, which may be on the order of years. On the other hand, time scales for changes in condensation clouds can be much faster. This gives support to the haze model, although this point is relatively weak.

Uranus and Titan share remarkable similarities. Both show banding structure but little discrete features, unlike other atmospheres dominated by cloud features. On Uranus and Titan, the banding structure is quite bland in the ultraviolet, becomes more obvious at longer wavelengths, especially at medium methane bands, but of lower contrast at strong methane bands. In both cases, the banding structure changes slowly with the seasons. Before the descent of Huygens onto Titan, vertical cloud structure models of Titan and Uranus were somewhat comparable, a high haze layer with mostly clear lower altitudes, except for possible condensation clouds, mostly by methane. However, the Huygens probe found haze all the way to the surface ([Tomasko et al., 2005](#)), and there was no major methane cloud although methane humidity data suggest that there should have been one ([Tokano et al., 2006](#)). Our data suggest the view of opacity in the atmosphere of Uranus may need to be revised in a similar way as for Titan through Huygens data. Huygens found the lower tropospheric visibility at visible wavelengths to be about 20 km, similar to our model for Uranus just below the 1.2 bar layer. Some of the research on Titan's atmosphere may be applicable to Uranus.

The haze model eliminates the discrepancy between the general circulation and the opacity of clouds. The general circulation based on radio data and the location of discrete features argues for rising air at low latitudes, while previous cloud layer models had the highest cloud opacity at high latitudes, which argued for the opposite circulation. Our haze model looks different from previous cloud layer models, but both kinds of models are observationally difficult to distinguish, in particular with two-dimensional data sets. The third dimension in our data set was helpful.

We may learn more by applying haze models to other data sets which have only been interpreted with cloud layer models. For example, [Sromovsky and Fry \(2008\)](#) noted that their model spectra do not perfectly fit observed spectra in the 1.28 μm region, where methane and hydrogen are both contributing to opacity providing a sensitive probe of the methane mixing ratio. Maybe, further analysis of the 1.28 μm band could confirm or contradict some of our ideas.

6.4. Model refinement

When we extended our analysis of the vertical structure to all of our 80 spectral samples and all of our six latitude regions, the simple two-parameter haze model still did reasonably well. However, systematic differences appeared which led us to a refinement of the model. First, the ultraviolet reflectivities and limb darkening required a very small amount of optical depth above the 1.2 bar layer. Thus, we added small amounts of stratospheric aerosols above the tropopause and tropospheric aerosols between the tropopause and the 1.2 bar layer.

This allowed very good fits for all wavelengths probing the higher altitudes. A systematic difference between observations and models remained in weak methane bands. On the left side of [Fig. 11](#), the shape of the curves varies gradually with methane absorption coefficient (top to bottom). This indicates that the latitudinal variation of the haze optical depth could not be the same at all altitudes below the 1.2 bar level. Thus, we divided this haze layer into two layers, and gave each layer its own latitudinal vari-

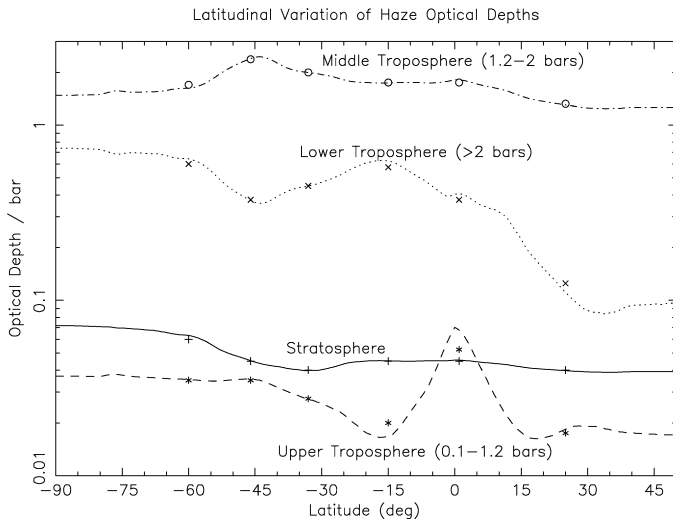


Fig. 21. Latitudinal variation of haze optical depths per bar of pressure, based on least-square fits to the whole data set (curves). Symbols mark our six latitude regions. The curve for stratospheric aerosols applies for an extinction efficiency of 0.1, corresponding to 900 nm wavelength. For 370 nm, it would shift upward by one order of magnitude.

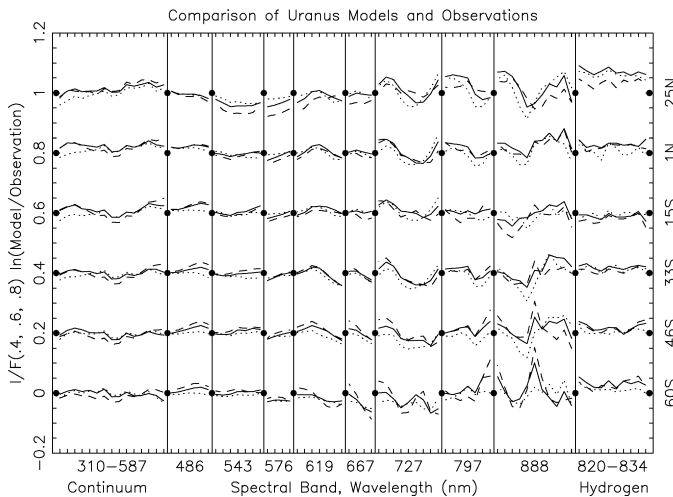


Fig. 22. Comparison of our 1440 data points with our radiative transfer model. The 80 tick marks at bottom correspond to our 80 spectral bands (cf. Table 2): 15 continuum wavelengths; 55 tick marks for methane absorptions in eight panels, each panel for one methane band, with increasing absorption coefficients from left to right within each panel; 10 tick marks for the hydrogen absorption region. Our six latitudinal regions are listed at the right edge. Dotted, dashed, and solid curves show the model reflectivities I_4/F , I_6/F , and I_8/F relative to the observations. The scale at left applies to latitude 60S and is offset by 0.2 successively. Solid dots mark the zero line for each latitude band, and one tick mark corresponds to 5%. The rms offset for all 1440 data points is 2%.

ation of optical depth. The dividing level between both layers was not well constrained, but the lowest residuals occurred for a dividing level around 2 bars, and we adopted this value. This allowed us to fit all curves with low residuals. Our best fits occurred for the lower layer having smaller optical depths per bar, especially at northern latitudes.

This refinement is not the only way to reduce residuals. Radiative transfer methods probe of the top unity optical depth of aerosols well, but they become unreliable further down. The only significant result about the lowest layer may be that northern latitudes were relatively clear.

Fig. 21 displays our adopted haze optical depth for six latitude regions and four altitude regions. Fig. 22 shows the residuals between observation and model for all 1440 data points. The rms

residual is 2% in reflectivity, a good fit between observation and model. We also included the model data in Figs. 11, 12, 14, and 16 as filled circles, yielding generally satisfying fits. Some areas in Fig. 22 hint to some systematic difference between observation and model since they are probably not systematic errors in the data. Residuals could be improved by adding free parameters to the model. Our model is simple, for example assuming that tropospheric aerosols are identical at all latitudes and all altitudes. Since most model parameters are correlated with each other in complicated ways, and since our model search did not fully cover the multi-dimensional parameter space, we cannot provide error bars for individual parameters.

While most previous radiative transfer calculations focused on less than our six latitude regions, we went one step further and provide radiative transfer models for all 140 latitude samples visible in 2002 (Fig. 21). Based on the results for the six latitude regions, we assumed linearity between model parameters and reflectivity to obtain the four optical depths at each latitude via a set of four linear equations. Checks at a few latitudes confirmed that our assumption was sufficiently accurate. Fig. 23 displays a summary of observations and the corresponding model images, displayed in identical contrast enhancement. The model images were convolved with the PSF of the reduced data to allow a consistent comparison. Generally, our radiative model explains most features. Thus, our model shows one possible explanation for the features on Uranus observed at wavelengths between 300 and 1000 nm.

7. Discrete clouds

The two brightest discrete clouds in our data set, one in each hemisphere, had reflectivity data as function of wavelength suitable for radiative modeling, but no limb darkening data. Both clouds were only observed with the G750L grating, providing data above 530 nm. We calculated the contrast, defined as the reflectivity enhancement relative to the background reflectivity.

Fig. 24 shows the observed and modeled contrasts at six methane bands. The model was based on Section 6.4 with additional opacity between the 1.2 bar level and a variable higher altitude. The additional optical depth needed to be around 0.2 for both clouds in order to yield the observed general contrasts, although this value depends on assumed aerosol parameters, which we adopted from Section 5. The top pressure level was constrained by the data points furthest left in Fig. 24. The northern cloud reached up very high, about to the tropopause, while the southern cloud had its opacity near the 1.2 bar level. This is qualitatively consistent with observations and models of previous discrete clouds (Karkoschka, 1998b; Sromovsky and Fry, 2005). The very different cloud top altitudes between the northern and southern cloud may suggest that they may be formed by different mechanisms. For example, southern clouds may be aerosols concentrated near the methane condensation level, while northern clouds may be condensation clouds. A better understanding will require models of cloud dynamics.

Both discrete clouds had low optical depths, even considering that the optical depth in the cloud center would be higher when accounting for the limited spatial resolution. The closest analog with clouds on Earth may be a cirrus cloud. Discrete clouds on Uranus could have holes like some cirrus clouds, which reduces reliability of results based on simple models like ours.

The models for the northern cloud are not perfect. The data of the 888 nm band are flatter than the model curves, and the wavelength dependence is not modeled well either. Models with smaller aerosols and decreasing opacity with altitude would improve the fits. We assumed methane to be independent of longitude, while the humidity could reach 100% in a discrete cloud

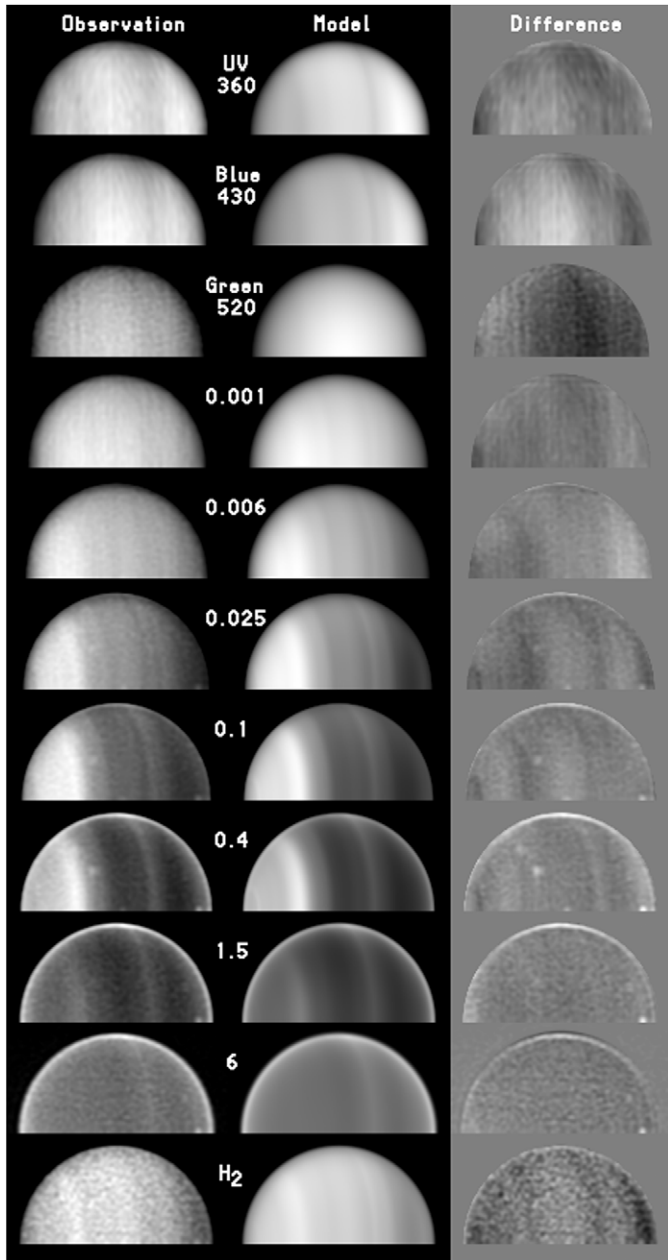


Fig. 23. Observations (left), synthetic images from our final radiative transfer model (center), and their difference three-fold enhanced (right) in 11 spectral regions: three continuum wavelengths, seven methane absorption coefficients as listed in km-am^{-1} , and one hydrogen absorption.

with rising air, which would require increased opacity at higher altitudes.

8. Summary

The three most powerful methods of radiative transfer involve observations of center-to-limb variations, methane bands of various strengths, and a wide spectral range. Center-to-limb data and methane band data have been successfully used in many investigations on Jovian planets. A wide spectral range probes different aspects of aerosols. In the ultraviolet, aerosols appear dark against bright Rayleigh scattering; in the near-infrared, aerosols appear bright against methane absorption. Our three-dimensional STIS data set allowed us to apply all three methods. It has 0.1 arc-sec spatial resolution and 1 nm spectral resolution between 300 and 1000 nm wavelength.

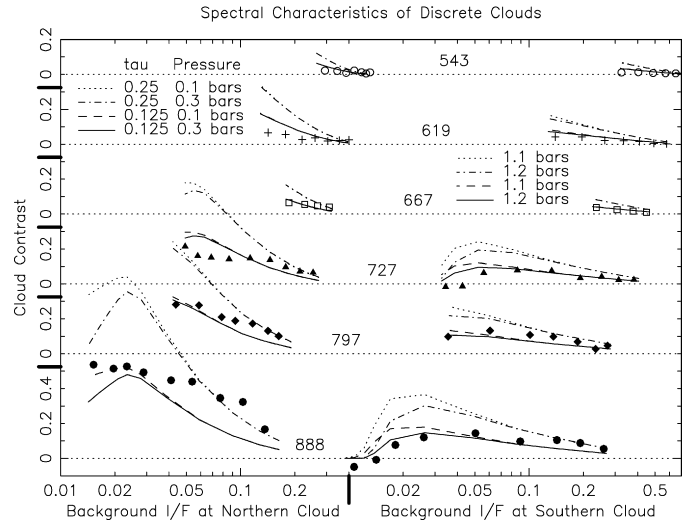


Fig. 24. Observed discrete cloud contrast (dots) in six methane bands for the northern (left) and southern cloud (right). Contrast is the relative enhancement of reflectivity over the background reflectivity. The curves show four models for each cloud which have additional opacity of 0.125 or 0.25 above the 1.2 bar layer with respect to the standard model at that latitude (cf. top left of figure). The opacity extends up to the 0.1 or 0.3 bar levels for the northern cloud and to 1.1 and 1.2 bar levels for the southern cloud. Uncertainties are about twice as large as the size of the symbols.

The full capabilities of this data set were obtained through accurate calibration, which was complicated but eventually successfully completed. Reflectivity and center-to-limb measurements agreed with those in images of 22 WFPC2 and ACS filters. Navigation was accurate to 0.002 arc-sec and 0.02 nm. The absolute reflectivity calibration was linked to the WFPC2 calibration (Karkoschka, 2001), accurate to 5%. Relative reflectivities were consistent with the WFPC2 and ACS data to the 1% level.

We reduced the data cube of 12 million data points to 1440 data points of four parameters: wavelength, methane absorption, latitude, and scattering geometry. These reduced data show the variation of reflectivity with one parameter for selected, constant values of other three parameters. This exceptional feature helped us to connect observed variations with physical parameters.

The large-scale vertical structure of Uranus has been established before. We confirmed that Uranus has very small aerosol opacity above the 1.2 bar level, but much larger opacity below. We also confirmed sizes of stratospheric aerosols ($\sim 0.1 \mu\text{m}$ radius) and the larger sizes of aerosols at deeper levels. If we assumed a model of two cloud layers below the 1.2 bar level according to Rages et al. (1991) and Baines et al. (1995), we roughly confirmed their cloud altitudes. Altitudes by Sromovsky and Fry (2007, 2008) and Irwin et al. (2007) were one scale height lower, based on data at longer wavelengths. This disagreement could be resolved by adjusting methane absorption coefficients similar to measurements in Titan's atmosphere (Tomasko et al., 2008), but the appropriate adjustment for Uranus is not known.

While most previous investigations assumed that the opacity at lower levels is concentrated in a few cloud condensation layers, our data fit haze layer models better than cloud layer models with the same number of free parameters. Our model has the opacity spread out in a smooth haze below the 1.2 bar level, thinning out partially at lower altitudes. We employed sensitive tests to detect distinct cloud layers, but found no evidence, considering that the vertical resolution of radiative transfer modeling is about half a scale height. Our data gave us other clues that Uranus has a thick, global, tropospheric haze, similar to Titan.

Our model reduces the hope that the mixing ratio of sulfur can be obtained by observing the level of a presumed H_2S cloud. Sromovsky and Fry (2007, 2008) suggested a possible observation of

this cloud, but the observed opacity could also have been part of the global haze.

Haze at lower altitudes displays a similar latitudinal distribution as haze at higher altitudes recorded a few years earlier, consistent with falling aerosols. This allows the first predictions of the future haze distribution, even more so if we understand aerosol production or growth, which may occur near the 1.2 bar level and be correlated with insulation. The north–south phase lag with respect to the 2007 equinox may soon be observed, which may indicate the mean falling time of aerosols from the production level to the mean level probed.

Based on the lack of data, most previous models of Uranus assumed that methane is uniformly mixed with latitude. The latitudinal brightness structure in methane band images was solely attributed to aerosol opacity variable with latitude. Previous tests of a possible latitudinal variation of methane were inconclusive (Sromovsky and Fry, 2008). We found a significant variability of methane with latitude, contradicting the key assumption. The latitudinal brightness structure seen in methane band images is not dominated by aerosol opacity, but by latitudinal variations in the methane mixing ratio in the 1.2–3 bar region. The ratio varies between 0.014 and 0.032 from high and low southern latitudes; both values are uncertain by about 20%, and their ratio by about 15%. The crucial data for obtaining these results were images in weak hydrogen absorptions, which are difficult to access with most observatories. Our surprising result may warrant reevaluating previous radiative transfer models, possibly even for Neptune.

The latitudinal structure of the methane mixing ratio is anti-correlated with the microwave brightness temperature, which probably tracks the ammonia mixing ratio at deeper levels (Hofstadter and Butler, 2003). The methane and ammonia variations may be causally related, which would provide important insight in the workings of the atmosphere.

Baines et al. (1995) suggested that the aerosols on Uranus may absorb significantly in the 600–1000 nm region. Our data indicate that aerosols on Uranus can be conservatively scattering in this region, similar to aerosols on Jupiter, Saturn, and Titan.

We present our radiative transfer results for all visible latitudes at the full spatial resolution of about 3°. We created synthetic images of Uranus based on our radiative transfer models, which agreed with observed reflectivities to 2% rms.

The upper layers of Uranus' atmosphere revealed one prominent feature, an equatorial zone. Its narrow aerosol opacity peak was centered on the equator to 0.2° accuracy. This feature may be related to influx of ring material onto Uranus. At lower altitudes, the feature was centered 1–2° further north, indicating northward meridional winds around the 1 bar level.

We found two, pronounced discrete clouds. The southern cloud had aerosol enhancement at the methane condensation level near 1.2 bars. The northern cloud reached two scale heights higher, close to the tropopause (0.1 bars). Both clouds were mostly transparent with optical depths around 0.2, although some areas within the clouds could have had much higher optical depths.

The unique capabilities of our data set allowed new results, but it lacked other important features such as the phase-angle coverage of Voyager or the time coverage of HST imaging. Adding these parameters to the new framework of radiative transfer models will yield progress in understanding Uranus. To encourage such work, we plan to post our three dimensional data sets, the fully calibrated and the Raman corrected one, on the Planetary Data System.

Acknowledgments

We thank Larry Sromovsky and Bob West for very helpful remarks about the manuscript. Support for this work was provided by NASA through grant numbers NAG5-12014 and NNX08AE74G,

and by the Space Telescope Science Institute through grant number HST-GO-09725.01-A.

References

- Baines, K.H., Mickelson, M.E., Larson, L.E., Ferguson, D.W., 1995. The abundances of methane and ortho/para hydrogen on Uranus and Neptune: Implications of new laboratory 4–0 H₂ quadrupole line parameters. *Icarus* 114, 328–340.
- Banfield, D., Gierasch, P.J., Bell, M., Ustinov, E., Ingersoll, A.P., Vasavada, A.R., West, R.A., Belton, M.J.S., 1998. Jupiter's cloud structure from Galileo imaging data. *Icarus* 135, 230–250.
- Borysov, J., Fu, Y., 2000. Semi-empirical model of collision-induced absorption spectra of H₂–H₂ complexes in the second overtone band of hydrogen at temperatures from 50 to 500 K. *Icarus* 145, 601–608.
- Colina, L., Bohlin, R.C., Castelli, F., 1996. The 0.12–2.5 micron absolute flux distribution of the Sun for comparison with solar analog stars. *Astron. J.* 112, 307–315.
- Conrath, R., Gautier, D., Hanel, R., Lindal, G., Marten, A., 1987. The helium abundance of Uranus from Voyager measurements. *J. Geophys. Res.* 92, 15003–15010.
- De Pater, I., Gibbard, S.G., Macintosh, B.A., Roe, H.G., Gavel, D.T., Max, C.E., 2002. Keck adaptive optics images of Uranus and its rings. *Icarus* 160, 359–374.
- Dressel, L., Aloisi, A., Diaz-Miller, R., Goudfrooij, P., Hodge, P., Holfeltz, S., Quijano, J.K., Maíz-Apellániz, J., Proffitt, C., 2007. STIS Data Handbook, Version 5.0. STScI, Baltimore.
- Fink, U., Benner, D.C., Dick, K.A., 1977. Band model analysis of laboratory methane absorption spectra from 4500 to 10500 Å. *J. Quant. Spectrosc. Radiat. Trans.* 18, 447–457.
- French, R.G., Elliot, J.L., French, L.M., Kangas, J.A., Meech, K.J., Ressler, M.E., Buie, M.W., Frogel, J.A., Holberg, J.B., Fuensalida, J.J., Joy, M., 1988. Uranian ring orbits from earth-based and Voyager occultation observations. *Icarus* 73, 349–378.
- French, R.G., Nicholson, P.D., Porco, C.C., Marouf, E.A., 1991. Dynamics and structure of the Uranian rings. In: Bergstrahl, J.T., Miner, E.D., Matthews, M.S. (Eds.), *Uranus*. Univ. of Arizona Press, Tucson, pp. 327–409.
- Fry, P.M., Sromovsky, L.A., 2007. Uranus cloud layers as constrained by HST STIS spectra. *Bull. Am. Astron. Soc.* 39, 526.
- Goudfrooij, P., Kimble, R.A., 2002. Correcting STIS CCD photometry for CTE loss. In: Arribas, S., Koekemoer, A., Whitmore, B. (Eds.), 2002 HST Calibration Workshop. STScI, Baltimore.
- Goudfrooij, P., Maíz-Apellániz, J., Brown, T., Kimble, R., 2006. Charge transfer efficiency of the STIS CCD: The time dependence of charge loss and centroid shifts from Internal Sparse Field data. Instrument Science Report STIS 2006-01. STScI, Baltimore.
- Hammel, H.B., de Pater, I., Gibbard, S.G., Lockwood, G.W., Rages, K., 2005. New cloud activity on Uranus in 2004: First detection of a southern feature at 2.2 µm. *Icarus* 175, 284–288.
- Hansen, J.E., 1971. Multiple scattering of polarized light in planetary atmospheres. II. Sunlight reflected by terrestrial water clouds. *J. Atmos. Sci.* 28, 1400–1426.
- Heney, L., Greenstein, J., 1941. Diffuse radiation in the galaxy. *Astrophys. J.* 93, 70–83.
- Hofstadter, M.D., Butler, B.J., 2003. Seasonal changes in the deep atmosphere of Uranus. *Icarus* 165, 168–180.
- Irwin, P.G.J., Sromovsky, L.A., Strong, E.K., Sihra, K., Teanby, N.A., Bowles, N., Calcutt, S.B., Remedios, J.J., 2006. Improved near-infrared methane band models and *k*-distribution parameters from 2000 to 9500 cm^{−1} and implications for interpretation of outer planet spectra. *Icarus* 181, 309–319.
- Irwin, P.G.J., Teanby, N.A., Davis, G.R., 2007. Latitudinal variations in Uranus' vertical cloud structure from UKIRT UIST observations. *Astrophys. J.* 665, L71–L74.
- Karkoschka, E., 1998a. Methane, ammonia, and temperature measurements of the Jovian planets and Titan from CCD-spectrophotometry. *Icarus* 133, 134–146.
- Karkoschka, E., 1998b. Clouds of high contrast on Uranus. *Science* 280, 570–572.
- Karkoschka, E., 2001. Comprehensive photometry of the rings and 16 satellites of Uranus with the Hubble Space Telescope. *Icarus* 151, 51–68.
- Karkoschka, E., Koekemoer, A., 2002. WFPC2 flatfields with reduced noise and an anomaly of filter FQCH4N-D. In: Arribas, S., Koekemoer, A., Whitmore, B. (Eds.), 2002 HST Calibration Workshop. Space Telescope Science Institute, Baltimore, pp. 315–324.
- Krist, J., 2004. The Tiny Tim User's Guide, Version 6.3. Space Telescope Science Institute, Baltimore.
- Lindal, G.F., Lyons, J.R., Sweetnam, D.N., Eshleman, V.R., Hinson, D.P., Tyler, G.L., 1987. The atmosphere of Uranus: Results of radio occultation measurements with Voyager 2. *J. Geophys. Res.* 92, 14987–15001.
- Lockwood, G.W., Jerzykiewicz, M., 2005. Photometric variability of Uranus and Neptune, 1950–2004. *Icarus* 180, 442–452.
- McGrath, M.A., Hodge, P., Baum, S., 1998. Calstis7: Two-dimensional rectification of spectroscopic data in the STIS calibration pipeline. Instrument Science Report STIS 98-13. STScI, Baltimore.
- Moses, J.I., Rages, K., Pollack, J.B., 1995. An analysis of Neptune's stratospheric haze using high-phase-angle Voyager images. *Icarus* 113, 232–266.
- Pryor, W.R., West, R.A., Simmons, K.E., 1997. High-phase-angle observations of Uranus at 2650 Å: Haze structure and particle properties. *Icarus* 127, 508–522.
- Rages, K.A., Hammel, H.B., Friedson, A.J., 2004. Evidence for temporal change at Uranus' south pole. *Icarus* 172, 548–554.

- Rages, K.A., Hammel, H.B., Sromovsky, L., 2007. Uranus: Direct comparison of northern vs. southern hemispheres at equinox. *Bull. Am. Astron. Soc.* 39, 425.
- Quijano, J.K., and 17 colleagues, 2007. STIS Instrument Handbook, Version 8.0. STScI, Baltimore.
- Rages, K., Pollack, J.B., Tomasko, M.G., Doose, L.R., 1991. Properties of scatterers in the troposphere and lower stratosphere of Uranus based on Voyager imaging data. *Icarus* 89, 359–376.
- Sromovsky, L.A., 2005. Accurate and approximate calculations of Raman scattering in the atmosphere of Neptune. *Icarus* 173, 254–283.
- Sromovsky, L.A., Fry, P.M., 2005. Dynamics of cloud features on Uranus. *Icarus* 179, 459–484.
- Sromovsky, L.A., Irwin, P.G.J., Fry, P.M., 2006. Near-IR methane absorption in outer planet atmospheres: Improved models of temperature dependence and implications for Uranus cloud structure. *Icarus* 182, 577–593.
- Sromovsky, L.A., Fry, P.M., 2007. Spatially resolved cloud structure on Uranus: Implications of near-IR adaptive optics imaging. *Icarus* 192, 527–557.
- Sromovsky, L.A., Fry, P.M., 2008. The methane abundance and structure of Uranus' cloud bands inferred from spatially resolved 2006 Keck grism spectra. *Icarus* 193, 252–266.
- Tokano, T., McKay, C.P., Neubauer, F.M., Atreya, S.K., Ferri, F., Fulchignoni, M., Niemann, H.B., 2006. Methane drizzle on Titan. *Nature* 442, 432–435.
- Tomasko, M.G., and 39 colleagues, 2005. Rain, winds and haze during the Huygens probe's descent to Titan's surface. *Nature* 438, 765–778.
- Tomasko, M.G., Bezaud, B., Doose, L., Engel, S., Karkoschka, E., 2008. Measurements of methane absorption by the descent imager/spectral radiometer (DISR) during its descent through Titan's atmosphere. *Planet. Space Sci.* 56, 624–647.
- West, R.A., 1991. Optical properties of aggregate particles whose outer diameter is comparable to the wavelength. *Appl. Opt.* 30, 5316–5324.